ARTICLE

https://doi.org/10.1038/s41586-019-1346-5

High-dimensional geometry of population responses in visual cortex

Carsen Stringer[1,2,6]*, Marius Pachitariu[1,3,6]*, Nicholas Steinmetz[3,5], Matteo Carandini[4,7] & Kenneth D. Harris[3,7]*

A neuronal population encodes information most efficiently when its stimulus responses are high-dimensional and uncorrelated, and most robustly when they are lower-dimensional and correlated. Here we analysed the dimensionality of the encoding of natural images by large populations of neurons in the visual cortex of awake mice. The evoked population activity was high-dimensional, and correlations obeyed an unexpected power law: the *n*th principal component variance scaled as $1/n$. This scaling was not inherited from the power law spectrum of natural images, because it persisted after stimulus whitening. We proved mathematically that if the variance spectrum was to decay more slowly then the population code could not be smooth, allowing small changes in input to dominate population activity. The theory also predicts larger power-law exponents for lower-dimensional stimulus ensembles, which we validated experimentally. These results suggest that coding smoothness may represent a fundamental constraint that determines correlations in neural population codes.

The visual cortex contains millions of neurons, and the patterns of activity that images evoke in these neurons form a 'population code'. The structure of this code is largely unknown, due to the lack of techniques that are able to record from large populations. Nonetheless, the population code is the subject of long-standing theories.

One such theory is the efficient coding hypothesis[1–3], which suggests that the neural code maximizes the transmission of information by eliminating correlations in natural image inputs. Such codes are high-dimensional and sparse, which can enable complex features to be read out by simple downstream networks[4–6].

However, several studies have suggested that neural codes are confined to low-dimensional subspaces (or 'planes')[7–15]. Codes of low planar dimension are correlated and redundant, allowing for robust computations of stimuli despite the presence of noise[16,17]. Nevertheless, low planar dimension is inevitable given stimuli or tasks of limited complexity[18]: the responses to a set of n stimuli, for example, have to lie in an n-dimensional subspace. The planar dimension of the cortical code thus remains an open question, which can only be answered by recording the responses of large numbers of neurons to large numbers of stimuli.

Here we recorded the simultaneous activity of approximately 10,000 neurons in the mouse visual cortex, in response to thousands of natural images. We found that stimulus responses were neither uncorrelated ('efficient coding') nor low-dimensional. Instead, responses occupied a multidimensional space, with the variance in the nth dimension scaling as a power law $n^{-\alpha}$, where $\alpha \approx 1$. We showed mathematically that if variances decay more slowly than a power law with exponent $\alpha = 1 + 2/d$, where d is the dimension of the input ensemble, then the space of neural activity must be non-differentiable—that is, not smooth. We varied the dimensionality of the stimuli d and found that the neural responses respected this lower bound. These findings suggest that the population responses are constrained by efficiency, to make best use of limited numbers of neurons, and smoothness, which enables similar images to evoke similar responses.

Simultaneous recordings of over 10,000 neurons

To obtain simultaneous recordings of approximately 10,000 cells from mouse V1, we used resonance-scanning two-photon calcium microscopy, using 11 imaging planes spaced at 35 μm (Fig. 1a). The slow time course of the GCaMP6s sensor enabled activity to be detected at a scan rate of 2.5 Hz, and an efficient data processing pipeline[19] yielded the activity of a large numbers of cells (Fig. 1b). Natural image scenes obtained from the ImageNet database[20] were presented on an array of three monitors surrounding the mouse (Fig. 1c), at an average of one image per second. Cells were tuned to these natural image stimuli: in experiments in which responses to 32 images were averaged over 96 repeats (Fig. 1d), stimulus responses accounted for 55.4 ± 3.3% (mean ± s.e.m., $n = 4$ recordings) of the trial-averaged variance. Consistent with previous reports[21–23], neuronal responses were sparse: only a small fraction of cells (13.4 ± 1.0%; mean ± s.e.m., $n = 4$ recordings) were driven more than two standard deviations above their baseline firing rate by any particular stimulus.

For our main experiments we assembled a sequence of 2,800 image stimuli. These stimuli were presented twice in the same order, to maximize the number of images presented while still allowing analyses based on cross-validation (Fig. 1e). Most neurons (81.4 ± 5.1%; mean ± s.e.m., $n = 7$ recordings) showed correlation between repeats at $P < 0.05$ (Extended Data Fig. 1a, b). Nevertheless, consistent with previous reports[24], the responses showed substantial trial-to-trial variability. Cross-validation showed that stimulus responses accounted for, on average, 13.2 ± 1.5% of the single-trial variance (Extended Data Fig. 1c), and the average signal-to-noise ratio was 17.3 ± 2.4% (Fig. 1f). This level of trial-to-trial variability was not due to our particular recording method: measuring responses to the same stimuli electrophysiologically yielded a similar signal-to-noise ratio (Extended Data Fig. 2). Despite this trial-to-trial variability, however, population activity recorded during a single trial contained substantial information about the sensory stimuli. A simple nearest-neighbour decoder, trained on one repeat and tested on the other, was able to identify the presented stimulus with up to 75.5% accuracy (Fig. 1g; range 25.4–75.5%; median

[1]HHMI Janelia Research Campus, Ashburn, VA, USA. [2]UCL Gatsby Computational Neuroscience Unit, University College London, London, UK. [3]UCL Institute of Neurology, University College London, London, UK. [4]UCL Institute of Ophthalmology, University College London, London, UK. [5]Present address: Department of Biological Structure, University of Washington, Seattle, WA, USA. [6]These authors contributed equally: Carsen Stringer, Marius Pachitariu. [7]These authors jointly supervised this work: Matteo Carandini, Kenneth D. Harris. *e-mail: stringerc@janelia.hhmi.org; pachitariu@janelia.hhmi.org; kenneth.harris@ucl.ac.uk

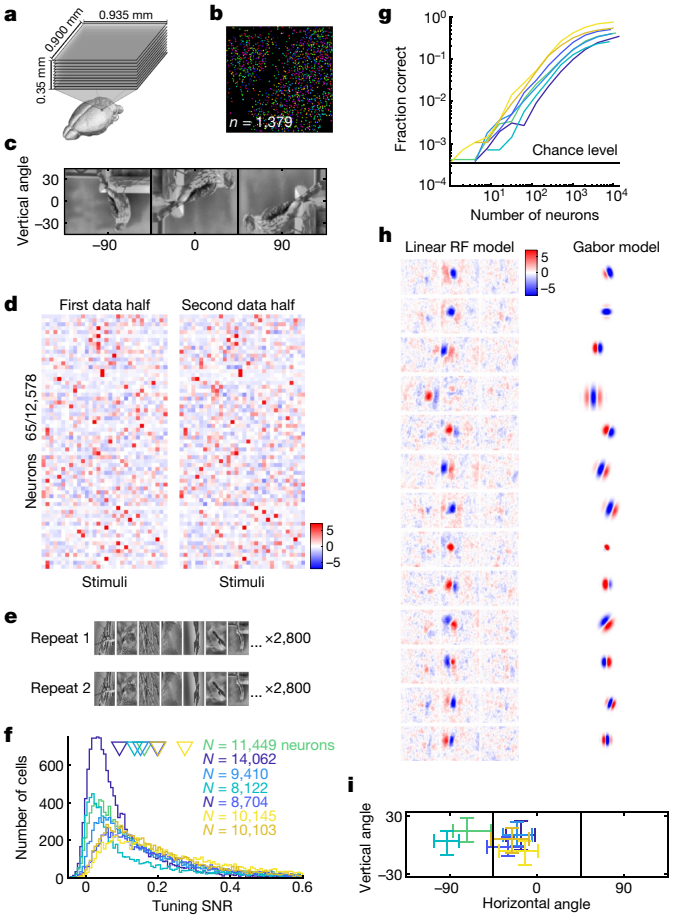

Fig. 1 | Population coding of visual stimuli. a, Simultaneous recording of approximately 10,000 neurons using 11-plane two-photon calcium imaging. **b**, Randomly pseudocoloured cells in an example imaging plane. **c**, An example stimulus spans three screens surrounding the head of the mouse. **d**, Mean responses (trial-averaged) of 65 randomly chosen neurons to 32 image stimuli (96 repeats, *z*-scored, scale bar represents standard deviations, one recording out of four is shown). **e**, A sequence of 2,800 stimuli was repeated twice during the recording. **f**, Neural stimulus tuning. The plot shows the distribution of single-cell signal-to-noise ratios (SNR) (2,800 stimuli, two repeats). Colours denote recordings; arrows represent means. **g**, Stimulus decoding accuracy as a function of neuron count for each recording. **h**, Example receptive fields (RFs) fit using reduced-rank regression or Gabor models (*z*-scored) (one recording shown, out of seven). **i**, Distribution of the receptive field centres, plotted on the left and centre screens (lines denote screen boundaries). Each cross represents a different recording, with 95% of the receptive field centres of the neurons within the error bars.

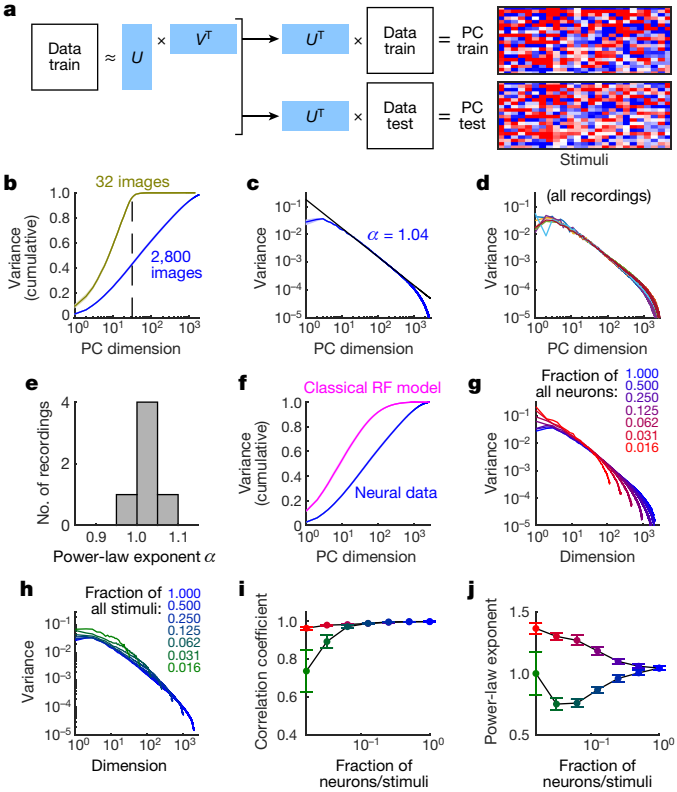

Fig. 2 | Visual cortical responses are high-dimensional with power-law eigenspectra. a, The eigenspectrum of visual stimulus responses was estimated by cvPCA, projecting singular vectors from the first repeat onto responses from the second. PC, principal component. **b**, Cumulative fraction of variance in planes of increasing dimension, for an ensemble of 2,800 stimuli (blue) and for 96 repeats of 32 stimuli (green). The dashed line indicates 32 dimensions. **c**, Eigenspectrum plotted in descending order of training-set singular value for each dimension, averaged across 7 recordings (shaded error bars represent s.e.m.). The black line denotes the linear fit of $1/n^{\alpha}$. **d**, Eigenspectra of each recording plotted individually. **e**, Histogram of power-law exponents α across all recordings. **f**, Cumulative eigenspectrum for a simple/complex Gabor model fit to the data (pink) superimposed on the true data (blue). **g**, Eigenspectra computed from random subsets of recorded neurons. Different colours indicate the different fractions of neurons. **h**, The same analysis as in **g**, but for random subsets of stimuli. **i**, Pearson correlation of log variance and log dimension over dimensions 11–500, as a function of fraction analysed (1 indicates a power law). **j**, Power-law exponents of the spectra plotted in **g**, **h**.

41.7% compared to a chance level of 0.036%, $n = 7$ recordings). The decoding accuracy did not saturate at a population size of 10,000, which suggests that performance would further improve with even larger neural populations.

The visual properties of neurons were consistent with those reported previously[23,25], and were highly diverse across the population. The responses of the neurons were only partially captured by classical linear–nonlinear models, which is consistent with previous studies of the visual cortex[26–30]. We calculated a receptive field for each cell from its responses to natural images in two ways: by fitting linear receptive fields regularized with a reduced-rank method; or by searching for an optimal Gabor filter that was rectified to simulate simple cell responses, and quadrature filtered to simulate complex cell responses. As expected[26–30], both receptive field models explained only a minor portion of the stimulus-related variance: the linear model explained 11.4 ± 0.7% (mean ± s.e.m.), and the Gabor model explained 18.5 ± 1.0% (mean ± s.e.m., $n = 7$ recordings each). As expected from retinotopy, there was overlap between the receptive field locations of simultaneously recorded neurons, but the sizes and shapes of the receptive fields were highly diverse (Fig. 1h, Extended Data Fig. 3).

Power–law scaling of dimensionality

To characterize the geometry of the population code for visual stimuli, we developed a method of cross-validated principal component analysis (cvPCA). cvPCA measures the reliable variance of stimulus-related dimensions, excluding trial-to-trial variability from unrelated cognitive and/or behavioural variables or noise. It accomplishes this by computing the covariance of responses between training and test presentations of an identical stimulus ensemble (Fig. 2a). Because only stimulus-related activity will be correlated across presentations, cvPCA provides an unbiased estimate of the stimulus-related variance. In simulations that use the same noise statistics as our recordings, we confirmed that this technique recovers the true variances (Extended Data Figs. 4, 5, Supplementary Discussion 1).

This method revealed that the visual population responses did not lie on any low-dimensional plane within the space of possible firing patterns. The amount of variance explained continued to increase as

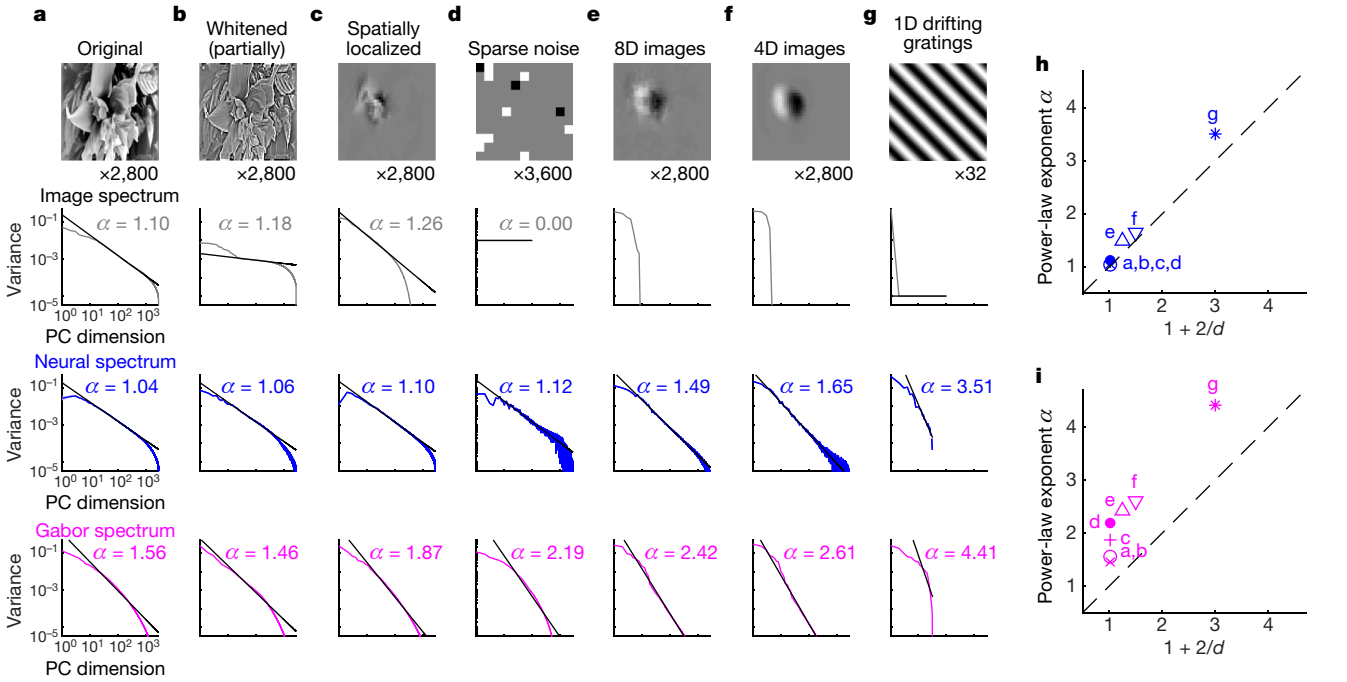

Fig. 3 | Power-law exponent depends on input dimensionality, but not on image statistics. a–g, Examples of presented images (top), eigenspectra of image pixel intensities (second row, grey), eigenspectra of visual cortical responses (third row, blue), and eigenspectra of responses of the Gabor receptive field model (fourth row, pink), for the original images (**a**), spatially whitened images lacking $1/n$ image spectrum (**b**), images windowed over the receptive field of the recorded population (**c**), sparse noise stimuli (**d**), images projected into eight dimensions, which produces a faster neural eigenspectrum decay with exponent $\alpha = 1.49$ (**e**), images projected into 4 dimensions, for which $\alpha = 1.65$ (**f**), drifting gratings, a one dimensional stimulus ensemble, for which $\alpha = 3.51$ (**g**). **h**, **i**, Summary of power-law exponents α for neural responses (**h**) and the Gabor model (**i**), as a function of the dimensionality of the stimulus set d. The dashed line, at $\alpha = 1 + 2/d$, corresponds to the border of fractality.

further dimensions were included, without saturating at any dimensionality below the maximum possible (Fig. 2b). As a control analysis, we applied cvPCA to the neural responses obtained when only 32 images were shown many times— the reliable component of these responses must, by definition, lie in a 32-dimensional subspace—and as expected we observed a saturation of the variance after 32 dimensions.

The analysis of our data using cvPCA revealed an unexpected finding: the fraction of neural variance in planes of successively larger dimensions followed a power law. The eigenspectrum—the function summarizing the variance of the nth principal component—had a magnitude that was approximately proportional to $1/n$ (Fig. 2c); this reflects successively less variance in dimensions that encode finer stimulus features (Extended Data Fig. 6). The power-law structure did not result from averaging over experiments: analysis of data from each mouse individually revealed power-law behaviour in every case (Fig. 2d). The scaling exponent of the power law was on average just above 1 (1.04 ± 0.02; mean $\pm$ s.e.m., $n = 7$ recordings, Fig. 2e). This eigenspectrum reflected correlations between neurons, and was not the consequence of a log-normal distribution of firing rates or signal variance (Extended Data Fig. 7). In addition, this result could not be explained by classical models of visual cortical receptive fields: the model of visual responses based on Gabor receptive fields with parameters fit to single cell responses (Fig. 1h) had lower dimensionality than the neural responses (Fig. 2f).

The range of dimensions over which the power law held grew with the number of neurons and stimuli that were analysed. To show this, we repeated the analyses on randomly chosen subsets of neurons or stimuli (Fig. 2g, h). Both the correlation coefficient and the slope (which represents the power-law exponent) approached 1 for increasing subset sizes (Fig. 2i, j, Extended Data Fig. 8). Electrophysiological recordings—with fewer recorded neurons and fewer presented stimuli—had the same eigenspectrum as a similarly-sized subset of the two-photon data (Extended Data Fig. 9). We conclude that the power law held accurately over approximately two orders of magnitude in these recordings, and we infer that it would probably extend further if more neurons and stimuli could be analysed.

Power-law and stimulus statistics

The power law followed by the neural eigenspectrum could not be explained by the well-known power-law structure of natural images[31,32] (Fig. 3a). To show this, we removed the image power law by spatially whitening the images, and presented the whitened stimuli to three of the mice. Although the power law in the image pixels was abolished, the power law in the neural responses remained (Fig. 3b). Furthermore, the eigenspectrum of neural responses could not be explained by straightforward receptive field properties: the model of visual responses based on Gabor receptive fields produced eigenspectra that decayed more quickly than the actual responses, and were worse fit by a power law ($P < 10^{-3}$, Wilcoxon rank-sum test on Pearson correlations, Fig. 3a, b).

The power-law eigenspectra also did not arise from other characteristics of natural images. To investigate the role of long-range image correlations, we constructed spatially localized image stimuli, in which the region outside the classical receptive field was replaced by grey. Again, the power law persisted with an exponent close to 1 (Fig. 3c). Finally, we removed any natural image structure and recorded responses to sparse noise stimuli (Fig. 3d). Again, we observed a power-law spectrum with an exponent close to 1 (1.13 ± 0.04; mean $\pm$ s.e.m., $n = 3$ recordings); although it was higher than for the natural image stimuli ($P = 0.067$, Wilcoxon two-sided rank-sum test). As with natural images, these power laws became more accurate the more neurons and stimuli were analysed (Extended Data Fig. 10). We therefore conclude that the power-law spectra exhibited by neural populations do not reflect the neural processing of a property that is specific to natural images.

Power-law and stimulus dimensionality

Power-law eigenspectra are observed in many scientific domains, and are related to the smoothness of the underlying functions. For example, if a function of one variable is differentiable, its Fourier spectrum must

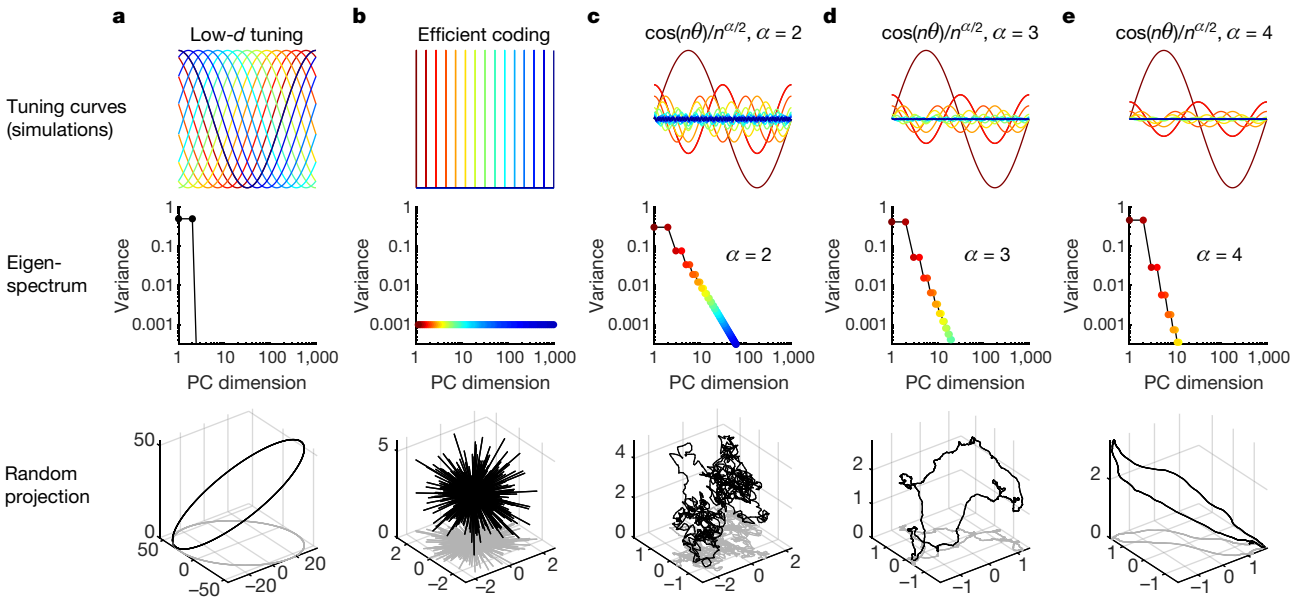

Fig. 4 | The smoothness of simulated neural activity depends on the eigenspectrum decay. Simulations of neuronal population responses to a one-dimensional stimulus (horizontal axis) (top), their eigenspectra (middle), and a random projection of population responses into three-dimensional space (bottom). **a**, Wide tuning curves, corresponding to a circular neural manifold in a two-dimensional plane. **b**, Narrow tuning curves corresponding to uncorrelated responses as predicted by the efficient coding hypothesis. **c**–**e**, Scale-free tuning curves corresponding to power-law variance spectra, with exponents of 2, 3 (the critical value for $d = 1$) or 4. The tuning curves in **c**–**e** represent PC dimensions rather than individual simulated neurons. Blue, dimensions that encode fine stimulus details; red, dimensions that encode large-scale stimulus differences.

decay asymptotically faster than a power law of exponent 1 (see, for example, a previously published study[33]). We therefore theorized that the variance power law might be related to smoothness of the neural responses. We showed mathematically that if the sensory stimuli presented can be characterized by d parameters, and if the mapping from these parameters to (noise-free) neural population responses is differentiable, then the population eigenspectrum must decay asymptotically faster than a power law of exponent $\alpha = 1 + 2/d$ (Supplementary Discussion 2). Conversely, if the eigenspectrum decays slower than this, a smooth neural code is impossible: its derivative tends to infinity with the number of neural dimensions, and the neural responses must lie on a fractal rather than a differentiable manifold.

This mathematical analysis gave rise to an experimental prediction. For a high-dimensional stimulus ensemble such as a set of natural images, d will be large and so $1 + 2/d \approx 1$, which is close to the exponent that we observed. However, for smaller values of d, the power law must have larger exponents if fractality is to be avoided. We therefore hypothesized that lower-dimensional stimulus sets would evoke population responses with larger power-law exponents. We obtained stimulus ensembles of dimensionality $d = 8$ and $d = 4$ by projecting the natural images onto a set of d basis functions (Fig. 3e, f). For a stimulus ensemble of dimensionality $d = 1$ we used drifting gratings, parameterized by a single direction variable. Consistent with the hypothesis, stimulus sets with $d = 8$, 4 and 1 yielded power-law scaling of eigenvalues with exponents of 1.49, 1.65 and 3.51, near but above the lower bounds of 1.25, 1.50 and 3.00 that are predicted by the $1 + 2/d$ exponent (Fig. 3h). The eigenspectra of simulated responses from a Gabor receptive field model fit to the data decayed even faster, suggesting a differentiable but lower-dimensional representation (Fig. 3i). These results suggest that the neural responses lie on a manifold that is almost as high-dimensional as is possible without becoming fractal.

Discussion

We found that the variance of the nth dimension of visual cortical population activity decays as a power of n, with exponent $\alpha \approx 1 + 2/d$ where d is the dimensionality of the space of sensory inputs. The population eigenspectrum reflects the fraction of neural variance that is devoted to representing coarse and fine stimulus features (Extended Data Fig. 6, Supplementary Discussion 2, 3). If the eigenspectrum were to decay slower than $n^{-1-2/d}$ then the neural code would emphasize fine stimulus features so strongly that it could not be differentiable. Our results therefore suggest that the eigenspectrum of the visual cortical code decays almost as slowly as is possible while still allowing smooth neural coding.

To illustrate the consequences of eigenspectrum decay for neural codes, we simulated various one-dimensional coding schemes in populations of 1,000 neurons, and visualized them by random projection into three-dimensional space (Fig. 4). The stimulus was parameterized by a single circular variable, such as the direction of a grating. A low-dimensional code with two non-zero eigenvalues produced a circular neural manifold (Fig. 4a). An uncorrelated, high-dimensional code in which each neuron responded to a different stimulus produced 1,000 equal variances, which is consistent with the efficient coding hypothesis (Fig. 4b). However this code did not respect distances: responses to stimuli separated by just a few degrees differed as much as responses to diametrically opposite stimuli, and the neural manifold appeared as a spiky, discontinuous ball. Power-law codes (Supplementary Discussion 2.7, example 2) show a scale-free geometry, the smoothness of which depends on the exponent α (Fig. 4c–e). A power-law code with $\alpha = 2$ (Fig. 4c) was a non-differentiable fractal because the many dimensions that encode fine stimulus details together outweighed the few dimensions that encode large-scale stimulus differences. At the critical exponent of $\alpha = 3$ (which is equal to $1 + 2/d$, because $d = 1$), the neural manifold was on the border of differentiability; the code represents fine differences between stimuli while still preserving large-scale stimulus features (Fig. 4d). A higher exponent led to a smoother neural manifold (Fig. 4e).

Neural representations with close-to-critical power-law eigenspectra may provide the brain with codes that are as efficient and flexible as possible while still allowing robust generalization. The efficient coding hypothesis suggests that information is optimally encoded when responses to different stimuli are as different as possible. However, such codes carry a cost: if the neural responses to any pair of stimuli were orthogonal, then stimuli that differ only in tiny details would have completely different representations (Supplementary Discussion 2.1). Similar behaviour can be seen in deep-neural-network architectures

that misclassify 'adversarial images' that differ imperceptibly from the training examples[34,35]. We suggest that a power-law code that is just above the critical exponent represents a balance between the efficiency of high-dimensional codes and the robustness of smooth codes, which enable generalization.

Online content

Any methods, additional references, Nature Research reporting summaries, source data, statements of data availability and associated accession codes are available at https://doi.org/10.1038/s41586-019-1346-5.

Received: 6 August 2018; Accepted: 29 May 2019;
Published online: 26 June 2019

1. Barlow, H. B. in *Sensory Communication* (ed. Rosenblith, W.) 217–234 (MIT Press, 1961).
2. Atick, J. J. & Redlich, A. N. Towards a theory of early visual processing. *Neural Comput.* **2**, 308–320 (1990).
3. Simoncelli, E. P. & Olshausen, B. A. Natural image statistics and neural representation. *Annu. Rev. Neurosci.* **24**, 1193–1216 (2001).
4. DiCarlo, J. J., Zoccolan, D. & Rust, N. C. How does the brain solve visual object recognition? *Neuron* **73**, 415–434 (2012).
5. Rigotti, M. et al. The importance of mixed selectivity in complex cognitive tasks. *Nature* **497**, 585–590 (2013).
6. Chung, S., Lee, D. D. & Sompolinsky, H. Classification and geometry of general perceptual manifolds. *Phys. Rev. X* **8**, 031003 (2018).
7. Cunningham, J. P. & Yu, B. M. Dimensionality reduction for large-scale neural recordings. *Nat. Neurosci.* **17**, 1500–1509 (2014).
8. Machens, C. K., Romo, R. & Brody, C. D. Functional, but not anatomical, separation of "what" and "when" in prefrontal cortex. *J. Neurosci.* **30**, 350–360 (2010).
9. Kobak, D. et al. Demixed principal component analysis of neural population data. *eLife* **5**, e10989 (2016).
10. Archer, E. W., Koster, U., Pillow, J. W. & Macke, J. H. Low-dimensional models of neural population activity in sensory cortical circuits. In *Proc. 27th International Conference on Neural Information Processing Systems* (eds Ghahramani, Z. et al.) 343–351 (Curran, 2014).
11. Sadtler, P. T. et al. Neural constraints on learning. *Nature* **512**, 423–426 (2014).
12. Chapin, J. K. & Nicolelis, M. A. Principal component analysis of neuronal ensemble activity reveals multidimensional somatosensory representations. *J. Neurosci. Methods* **94**, 121–140 (1999).
13. Bathellier, B., Buhl, D. L., Accolla, R. & Carleton, A. Dynamic ensemble odor coding in the mammalian olfactory bulb: sensory information at different timescales. *Neuron* **57**, 586–598 (2008).
14. Churchland, M. M. et al. Neural population dynamics during reaching. *Nature* **487**, 51–56 (2012).
15. Mante, V., Sussillo, D., Shenoy, K. V. & Newsome, W. T. Context-dependent computation by recurrent dynamics in prefrontal cortex. *Nature* **503**, 78–84 (2013).
16. Shadlen, M. N. & Newsome, W. T. The variable discharge of cortical neurons: implications for connectivity, computation, and information coding. *J. Neurosci.* **18**, 3870–3896 (1998).
17. Reich, D. S., Mechler, F. & Victor, J. D. Independent and redundant information in nearby cortical neurons. *Science* **294**, 2566–2568 (2001).
18. Gao, P. et al. A theory of multineuronal dimensionality, dynamics and measurement. Preprint at https://www.biorxiv.org/content/early/2017/11/12/214262 (2017).
19. Pachitariu, M. et al. Suite2p: beyond 10,000 neurons with standard two-photon microscopy. Preprint at https://www.biorxiv.org/content/early/2017/07/20/061507 (2016).
20. Deng, J. et al. Imagenet: A large-scale hierarchical image database. In *IEEE Conference on Computer Vision and Pattern Recognition* 248–255 (IEEE, 2009).
21. Vinje, W. E. & Gallant, J. L. Natural stimulation of the nonclassical receptive field increases information transmission efficiency in V1. *J. Neurosci.* **22**, 2904–2915 (2002).
22. Ringach, D. L. Spatial structure and symmetry of simple-cell receptive fields in macaque primary visual cortex. *J. Neurophysiol.* **88**, 455–463 (2002).
23. Niell, C. M. & Stryker, M. P. Highly selective receptive fields in mouse visual cortex. *J. Neurosci.* **28**, 7520–7536 (2008).
24. Softky, W. R. & Koch, C. The highly irregular firing of cortical cells is inconsistent with temporal integration of random EPSPs. *J. Neurosci.* **13**, 334–350 (1993).
25. Cossell, L. et al. Functional organization of excitatory synaptic strength in primary visual cortex. *Nature* **518**, 399–403 (2015).
26. Smyth, D., Willmore, B., Baker, G. E., Thompson, I. D. & Tolhurst, D. J. The receptive-field organization of simple cells in primary visual cortex of ferrets under natural scene stimulation. *J. Neurosci.* **23**, 4746–4759 (2003).
27. Carandini, M. et al. Do we know what the early visual system does? *J. Neurosci.* **25**, 10577–10597 (2005).
28. David, S. V. & Gallant, J. L. Predicting neuronal responses during natural vision. *Netw. Comput. Neural Syst* **16**, 239–260 (2005).
29. Touryan, J., Felsen, G. & Dan, Y. Spatial structure of complex cell receptive fields measured with natural images. *Neuron* **45**, 781–791 (2005).
30. de Vries, S. E. J. et al. A large-scale, standardized physiological survey reveals higher order coding throughout the mouse visual cortex. Preprint at https://www.biorxiv.org/content/early/2018/06/29/359513 (2018).
31. Field, D. J. Relations between the statistics of natural images and the response properties of cortical cells. *J. Opt. Soc. Am. A* **4**, 2379–2394 (1987).
32. Ruderman, D. L. & Bialek, W. Statistics of natural images: Scaling in the woods. In *Advances in Neural Information Processing Systems* 551–558 (1994).
33. Tao, T. *An Epsilon of Room, I: Real Analysis* 1.12.3 (American Mathematical Society, 2010).
34. Szegedy, C. et al. Intriguing properties of neural networks. Preprint at http://arxiv.org/abs/1312.6199 (2013).
35. Goodfellow, I. J., Shlens, J. & Szegedy, C. Explaining and harnessing adversarial examples. Preprint at http://arxiv.org/abs/1412.6572 (2014).

Acknowledgements We thank M. Krumin for assistance with the two-photon microscopes, C. Reddy for surgeries, and K. Falconer, A. Gretton and M. Benna for discussions of mathematics. This research was funded by Wellcome Trust Investigator grants (108726, 205093 and 204915) and by a grant from the Simons Foundation (SCGB 325512). C.S. was funded by a four-year Gatsby Foundation PhD studentship. M.C. holds the GlaxoSmithKline/Fight for Sight Chair in Visual Neuroscience. K.D.H. was funded by the European Research Council (694401). N.S. was supported by postdoctoral fellowships from the Human Frontier Sciences Program and the Marie Curie Action of the EU (656528). C.S. and M.P. are now funded by HHMI Janelia.

Reviewer information *Nature* thanks Jakob Macke, Ken Miller and Byron Yu for their contribution to the peer review of this work.

Author contributions C.S., M.P., N.S., M.C. and K.D.H. conceptualized the study; C.S., M.P., N.S. and K.D.H. devised the methodology; C.S. and M.P. designed the software; C.S., M.P. and N.S. performed experiments; C.S. and M.P. analysed the data; K.D.H. proved mathematical theorems; C.S., M.P., N.S., M.C. and K.D.H. wrote the paper; and M.C. and K.D.H. provided resources and acquired funding.

Competing interests The authors declare no competing interests.

Additional information
Extended data is available for this paper at https://doi.org/10.1038/s41586-019-1346-5.
Supplementary information is available for this paper at https://doi.org/10.1038/s41586-019-1346-5.
Reprints and permissions information is available at http://www.nature.com/reprints.
Correspondence and requests for materials should be addressed to C.S., M.P. or K.D.H.
Publisher's note: Springer Nature remains neutral with regard to jurisdictional claims in published maps and institutional affiliations.

METHODS

All experimental procedures were conducted according to the UK Animals Scientific Procedures Act (1986). Experiments were performed at University College London under personal and project licenses released by the Home Office following appropriate ethics review.

Animals and surgery. We used mice that were bred to express GCaMP6s in excitatory neurons in our recordings: 13 recordings from TetO-GCaMP6s × Emx1-IRES-Cre mice (available as JAX 024742 and JAX 005628); 3 recordings from a Camk2a-tTA, Ai94 GCaMP6s 2tg × Emx1-IRES-Cre mouse (available as JAX 024115 and JAX 005628); and 2 recordings from a Camk2a-tTA, Ai94 GCaMP6s 2tg × Rasgrf-Cre mouse (available as JAX 024115 and JAX 022864). We also used mice bred to express tdTomato in inhibitory neurons (GAD-IRES-Cre × CAG-tdTomato, available as JAX 010802 and JAX 007909) in 14 recordings. In this case, GCaMP6s was expressed virally, and excitatory neurons were identified by lack of tdTomato expression. These mice were male and female, with ages ranging from 2 months to 8 months. We recorded from sufficient mice to draw scientific conclusions (8 mice in total). There was no randomization or blinding done in the study.

Surgical methods were similar to those described elsewhere[19,36]. In brief, surgeries were performed in adult mice (postnatal day (P)35–P125) under isoflurane anaesthesia (5% for induction, 0.5–1% during the surgery) in a stereotaxic frame. Before surgery, Rimadyl was administered as a systemic analgesic and lidocaine was administered locally at the surgery site. During the surgery we implanted a head-plate for subsequent head-fixation, and made a craniotomy of 3–4 mm in diameter with a cranial window implant for optical access. In Gad-Cre × tdTomato transgenic mice, we targeted virus injections (AAV2/1-hSyn-GCaMP6s, University of Pennsylvania Vector Core, 50–200 nl, 1–3 × 10^{12} GC ml^{-1}) to monocular V1 (2.1–3.3 mm laterally and 3.5–4.0 mm posteriorly from bregma), using a beveled micropipette and a Nanoject II injector (Drummond Scientific Company) attached to a stereotaxic micromanipulator. To obtain large fields of view for imaging, we typically performed 4–8 injections at nearby locations, at multiple depths (around 500 μm and around 200 μm). Rimadyl was then used as a post-operative analgesic for three days, and was delivered to the mice through their drinking water.

Data acquisition. We used a two-photon microscope (Bergamo II multiphoton imaging microscope, Thorlabs) to record neural activity, and ScanImage[37] for data acquisition, obtaining 10,622 ± 1,690 (mean ± s.d.) neurons in the recordings. The recordings were performed using multi-plane acquisition controlled by a resonance scanner, with planes spaced 30–35 μm apart in depth. Ten or twelve planes were acquired sequentially, scanning the entire stack repeatedly at 3 Hz or 2.5 Hz. Because plane scanning was not synchronized to stimulus presentation, we aligned the stimulus onsets to each of the planes separately, and computed stimulus responses from the first two frames acquired after stimulus onset for each plane.

The mice were free to run on an air-floating ball and were surrounded by three computer monitors arranged at 90° angles to the left, front and right of the mouse, so that the head of the mouse was approximately in the geometric centre of the setup. Data from running and non-running periods were analysed together.

For each mouse, recordings were made over multiple days, always returning to the same field of view (in one mouse, two fields of view were used). For each mouse, a field of view was selected on the first recording day such that 10,000 neurons could be observed, with clear calcium transients and a retinotopic location (identified by neuropil fluorescence) localized on the monitors. If more than one potential field of view satisfied these criteria, we chose either a horizontally and vertically central retinotopic location, or a lateral retinotopic location, at 90° from the centre but still centred vertically. The retinotopic location of the field of view (central or lateral) was unrelated to variance spectra. We also did not observe differences between recordings obtained from different modes of GCaMP expression (transgenic versus viral injection). Thus, we pooled data over all conditions.

Visual stimuli. During two-photon recordings, all stimuli other than sparse noise stimuli were presented for 0.5 s, alternating with a grey-screen inter-stimulus interval lasting a random time between 0.3 and 1.1 s. During electrophysiological recordings, all stimuli were presented for 400 ms, with a uniformly distributed inter-stimulus interval of 300–700 ms.

Image stimuli were selected from the ImageNet database[20], from ethologically relevant categories: 'birds', 'cat', 'flowers', 'hamster', 'holes', 'insects', 'mice', 'mushrooms', 'nests', 'pellets', 'snakes' and 'wildcat'. Images were chosen manually to ensure that less than 50% of the image was a uniform background, and to contain a mixture of low and high spatial frequencies. The images were uniformly contrast-normalized. This was achieved by subtracting the local mean brightness and dividing by the local mean contrast (standard deviation of pixel values); the local mean and standard deviation were both computed using a Gaussian filter of standard deviation 30°. Each presented stimulus consisted of a different normalized image from ImageNet (2,800 different images) replicated across all three screens, but at a different rotation on each screen (Fig. 1c).

For the main two-photon recordings, these 2,800 stimuli were presented twice, in the same order each time. In the electrophysiological recordings, 700 of these same stimuli were presented twice in the same order each time. Additionally, in a subset of imaged mice (4 out of 6), we presented a smaller set of 32 images, presented in a randomized order 90–114 times, to enable more accurate estimation of trial-averaged responses.

We also presented partially spatially whitened versions of the 2,800 natural images. To compute spatially whitened images, we first computed the two-dimensional Fourier spectrum for each image, and averaged the spectra across images. We then whitened each image in the frequency domain by dividing its Fourier transform by the averaged Fourier spectrum across all images with a small constant value added for regularization purposes. The rescaled Fourier transform of the image was transformed back into the pixel domain by computing its inverse two-dimensional Fourier transform and retaining the real part. Each image was then intensity-scaled to have the same mean and standard deviation pixel values as the original.

The eight- and four-dimensional stimuli were constructed using a reduced-rank regression model. We first used reduced-rank regression to predict the neuronal population responses R from the natural images I ($N_{\text{pixels}} \times N_{\text{stimuli}}$) via a d-dimensional bottleneck:

$$R = A^{\mathrm{T}} BI$$

where A is a matrix of size $d \times N_{\text{neurons}}$ and B is a matrix of size $d \times N_{\text{pixels}}$. The dimensionality d was either eight or four depending on the set of stimuli being constructed. The columns of B represent the image dimensions that linearly explain the most variance in the neural population responses. The stimuli were the original 2,800 natural images projected onto the reduced-rank subspace B: $I_{\text{low-}d} = B^{\mathrm{T}}BI$.

In addition to natural image stimuli, we also presented drifting gratings and sparse noise. Drifting gratings of 32 directions, spaced evenly at 11.25°, were presented 70–128 times each, lasting 0.5 s each, and with a grey-screen inter-stimulus interval between 0.3 and 1.1 s. They were full-field stimuli (all three monitors) and their spatial frequency was 0.05 cycles per degree and their temporal frequency was 2 Hz.

Sparse noise stimuli consisted of white or black squares on a grey background. Squares were of size 5°, and changed intensity every 200 ms. On each frame, the intensity of each square was chosen independently, as white with 2.5% probability, black with 2.5% probability, and grey with 95% probability. The sparse noise movie contained 6,000 frames, lasting 20 min, and the same movie was played twice to allow cross-validated analysis.

Spontaneous activity was recorded for 30 min with all monitors showing a grey or black background, in all but six of 32 image set recordings. In three recordings of 32-natural image responses and three recordings of drifting grating responses, we interspersed the spontaneous activity, recording 30 s of spontaneous grey-screen activity in between each set of 32 stimuli. In all recordings but these 6, there were also occasional blank stimuli (1 out of every 20 stimuli in the 2,800 natural image stimuli). The activity during these non-stimulus periods was used to project out spontaneous dimensions from the neuronal population responses (see below).

Calcium imaging processing. Calcium movie data was processed using the Suite2p toolbox[19,36], available at https://www.github.com/cortex-lab/Suite2P.

In brief, the Suite2p pipeline consists of registration, cell detection, region of interest (ROI) classification, neuropil correction and spike deconvolution. Movie frames are registered using 2D translation estimated by regularized phase correlation, subpixel interpolation and kriging. To detect ROIs (corresponding to cells), Suite2p clusters correlated pixels, using a low-dimensional decomposition of the data to accelerate processing. The number of ROIs is determined automatically by a threshold on pixel correlations. Finally, ROIs were classified as somatic or non-somatic using a classifier trained on a set of human-curated ROIs. The classifier reached 95% agreement on test data, thus allowing us to skip manual curation for most recordings. For neuropil correction, we used a previously published approach[38], subtracting from each ROI signal the surrounding neuropil signal scaled by a factor of 0.7; all pixels attributed to an ROI (somatic or not) were excluded from the neuropil trace. After neuropil subtraction, we further subtracted a running baseline of the calcium traces with a sliding window of 60 s to remove long-timescale additive baseline shifts in the signals. Fluorescence transients were estimated using non-negative spike deconvolution[39] with a fixed timescale of calcium indicator decay of 2 s, a method that we found to outperform others on ground-truth data[40]. Finally, the deconvolved trace of each cell was z-scored with respect to the mean and standard deviation of the trace of that cell during a 30-min period of grey-screen spontaneous activity before or after the image presentations.

All of the processed deconvolved calcium traces are available on figshare[41] (https://figshare.com/articles/Recordings_of_ten_thousand_neurons_in_visual_cortex_in_response_to_2_800_natural_images/6845348), together with the image stimuli.

Data acquisition and processing (electrophysiology). Neuropixels electrode arrays[42] were used to record extracellularly from neurons in six mice. The mice were between 8 weeks old and 24 weeks old at the time of recording, and were of either sex. The genotypes of the mice were Slc17a7-Cre;Ai95, Snap25-GCaMP6s, TetO-GCaMP6s;CaMKIIa-tTA, Ai32;Pvalb-Cre (two mice), or Emx1-Cre;CaMKIIa-tTA;Ai94. In some cases, other electrophysiological recordings had been made from other locations in the days preceding the recordings reported here. In all cases, a brief (less than 1 h) surgery to implant a steel headplate and 3D-printed plastic recording chamber (12-mm diameter) was first performed. After recovery, mice were acclimatized to head-fixation in the recording setup. During head-fixation, mice were seated on a plastic apparatus with forepaws on a rotating rubber wheel (five mice) or were on a Styrofoam treadmill and able to run (one mouse). Three 20 × 16 cm TFT-LCD screens (LG LP097QX1) were positioned around the mouse at right angles at a distance of 10 cm, covering a total visual angle of 270 × 78 degrees. On the day of recording, mice were again briefly anaesthetized with isoflurane while up to eight small craniotomies were made with a dental drill. After several hours of recovery, mice were head-fixed in the set-up. Probes had a silver wire soldered onto the reference pad and shorted to ground; these reference wires were connected to a Ag/AgCl wire positioned on the skull. The craniotomies as well as the wire were covered with saline-based agar. The agar was covered with silicone oil to prevent drying. Probes were each mounted on a rod held by an electronically positionable micromanipulator (uMP-4, Sensapex) and were then advanced through the agar and through the dura. Once electrodes punctured the dura, they were advanced slowly (10 μm s^{-1}) to their final depth (4 or 5 mm deep). Electrodes were allowed to settle for approximately 15 min before starting recording. Recordings were made in external reference mode with local field potential (LFP) gain = 250 and action potential (AP) gain = 500, using SpikeGLX software. Data were preprocessed by re-referencing to the common median across all channels. Six recordings were performed in six different mice, with a total of 14 probes in visual cortex across all experiments.

We spike-sorted the data using a modification of Kilosort[43] that tracks drifting clusters, called Kilosort2[36,44], available at https://www.github.com/MouseLand/Kilosort2. Without the modifications, the original Kilosort and similar algorithms can split clusters according to drift of the electrode. Kilosort2, in comparison, tracks neurons across drift levels and for longer periods of time (around 1 h in our case).

Removal of ongoing activity dimensions. As shown previously[36], approximately half of the shared variance of visual cortical population activity is unrelated to visual stimuli, but represents behaviour-related fluctuations. This ongoing activity continues uninterrupted during stimulus presentations, and overlaps with stimulus responses only along a single dimension. Because the present study is purely focused on sensory responses, we projected out the dimensions corresponding to ongoing activity before further analysis. The top 32 dimensions of ongoing activity were found by performing a PCA on the z-scored ongoing neural activity recorded during a 30-min period of grey-screen stimuli before or after the image presentations. To remove these dimensions from stimulus responses, the stimulus-driven activity was also first z-scored (using the mean and variance of each neuron computed from spontaneous activity), then the projection onto the 32 top spontaneous dimensions was subtracted (Extended Data Fig. 4).

In the electrophysiological recordings, we considered stimulus responses in a window of 50 ms or 500 ms following stimulus onset. Therefore, we computed the ongoing activity using these two different bin sizes (50 ms or 500 ms). Then we z-scored the stimulus responses by this ongoing activity. Next we computed the top ten PCs of the ongoing activity (in both bin sizes) and then subtracted the projection of the stimulus responses onto these dimensions.

Receptive field estimation. We estimated the receptive fields of the neurons, either using a reduced-rank regression model or using a simple/complex Gabor model. In both cases, the model was fitted to the mean response of each neuron to half of the 2,800 images (I_{train}) over the two repeats. The performance of the model was tested on the mean response of each neuron to the other half of the 2,800 images (I_{test}).

Reduced-rank receptive field estimation. To estimate a linear receptive field for each neuron, we used reduced-rank regression[45], a self-regularizing method that allowed us to fit the responses of all neurons to a single repeat of all 2,800 image stimuli. Reduced-rank regression predicts high-dimensional outputs from high-dimensional inputs through a linear low-dimensional hidden 'bottleneck' representation. We used a 25-dimensional hidden representation to predict the activity of each neuron from the image pixel vectors, taking the resulting regressor matrices as the linear receptive fields. These receptive fields explained 11.4 ± 0.7% (mean ± s.e.m., $n = 7$ recordings) of the stimulus-related variance on the test set. These were z-scored before display in Fig. 1h and Extended Data Fig. 3a.

Model-based receptive field estimation. To fit classical simple/complex receptive fields to each cell, we simulated the responses of a convolutional grid of Gabor filters to the natural images, and fit each neuron with the filter response most correlated to its response.

The Gabor cell filters $G(\boldsymbol{x})$ were parametrized by a spatial frequency f, orientation θ, phase ψ, size α and eccentricity β. Defining $\boldsymbol{u}$ and $\boldsymbol{v}$ to be unit vectors pointing parallel and perpendicular to the orientation θ:

$$G(\boldsymbol{x}) = \cos(2\pi f \boldsymbol{x}\cdot\boldsymbol{u} + \psi)\mathrm{e}^{-((\boldsymbol{x}\cdot\boldsymbol{u})^2+\beta(\boldsymbol{x}\cdot\boldsymbol{v})^2)/2\alpha^2}$$

We constructed 12,288 Gabor filters, with centres spanning a 9 by 7 grid spaced at 5 pixels, and with parameters f, θ, ϕ, α and β ranging from (0.01, 0, 0, 3, 1) to (0.13, 157, 315, 12, 2.5) with (7, 8, 8, 4, 4) points sampled of each parameter, respectively. The parameters were equally spaced along the grid (for example, f was sampled at 0.01, 0.03, 0.05, 0.07, 0.09, 0.11, 0.13).

Simple cell responses were simulated by passing the dot product of the image with the filter through a rectifier function $r(x) = \max(0, x)$. Complex cell responses were simulated as the root-mean-square response of each unrectified simple cell filter and the same filter with phase ψ shifted by 90°. The activity of a neuron was predicted as a linear combination of a simple cell and its complex cell counterpart, with weights estimated by linear regression. Each neuron was assigned to the filter which best predicted its responses to the training images (Extended Data Fig. 3b–h). This simple/complex Gabor model explained 18.4 ± 0.1% (mean ± s.e.m.) of the stimulus-related variance on the test set.

We also evaluated a model of Gabor receptive fields including divisive normalization[46]. To do so, the response of each of the modelled simple or complex cell filters was divided by the summed, normalized responses of all the other simple and complex cells at this retinotopic location. The experimentally measured response of each neuron was then predicted as a linear combination of simple and complex responses to the best-fitting Gabor, with weights estimated by linear regression. In total, 45.4% ± 1.0% (mean ± s.e.m.) of cells were better fit by the divisive normalization model. However, although divisive normalization changed the optimal parameters fit to many cells (Extended Data Fig. 3i–n), the resulting eigenspectra were indistinguishable from a model with no normalization (Extended Data Fig. 3o–u).

Sparseness estimation. To estimate the sparseness of single-cell responses to the image stimuli, we counted how many neurons were driven more than two standard deviations above their baseline rate by any given stimulus. This was estimated using 4 experiments in which 32 natural images were repeated more than 90 times. We computed the tuning curve of each neuron by averaging over all repeats. The standard deviation of the tuning curve is computed for each neuron across stimuli. The baseline rate was defined as the mean firing rate during all spontaneous activity periods, without visual stimuli. A neuron was judged as responsive to a given stimulus if its response was more than two times this standard deviation plus its baseline firing rate.

Decoding accuracy from 2,800 stimuli. To decode the stimulus identity from the neural responses (Fig. 1g), we built a simple nearest-neighbour decoder based on correlation. The first stimulus presentation was used as the training set while the second presentation was used as the test set. We correlated the population responses for an individual stimulus in the test set with the population responses from all stimuli in the training set. The stimulus with the maximum correlation was then assigned as our prediction. We defined the decoding accuracy as the fraction of correctly labelled stimuli.

Signal-to-noise ratio and explained variance. To compute the tuning-related SNR (Fig. 1f), we first estimated the signal variance of each neuron $\hat{V}_{\text{sig}}$ as the covariance of its response to all stimuli across two repeats (for neuron c, $\hat{V}_{\text{sig}} = \mathrm{Cov}_s[f_1(c,s), f_2(c,s)]$ where $f_r(c,s)$ is the response of neuron c to stimulus s on repeat r, see Supplementary Discussion 1). The noise variance $\hat{V}_{\text{noise}} = V_{\text{tot}} - \hat{V}_{\text{sig}}$ was defined as the difference between the within-repeat variance (reflecting both signal and noise) and this signal variance estimate, and the SNR was defined as their ratio. The SNR estimate is positive when a neuron has responses to stimuli above its noise baseline; note that as $\hat{V}_{\text{sig}}$ is an unbiased estimate, it can take negative values when the true signal variance is zero.

To compute the percentage of explained variance for each neuron (Extended Data Fig. 1c), we divided the estimated signal variance by the total variance across trials (averaged across the repeats):

$$\mathrm{EV} = \frac{\hat{V}_{\text{sig}}}{\frac{1}{2}(\mathrm{Var}_s[f_1(c,s)] + \mathrm{Var}_s[f_2(c,s)])}$$

Note that this formula is similar to the Pearson correlation of the responses of a neuron between two repeats. In the Pearson correlation the numerator is the same, equal to the covariance between repeats, but the denominator is the geometric rather than arithmetic mean of the variances of the two repeats.

cvPCA method. The cvPCA method is fully described in Supplementary Discussion 1, characterized mathematically in Supplementary Discussion 1.1 and 3.6, and analysed in simulation in Extended Data Fig. 5. In brief, the difference between this approach and standard PCA (for example, see previous studies[47,48]) is that it compares the activity on training and test repeats to obtain an estimate

of the stimulus-related ('signal') variance, discounting variance from trial-to-trial variability ('noise').

Denote the response of neuron c to repeat r of stimulus s by $f_r(c, s)$, define the signal as the expected response, which will be equal for both repeats: $\phi(c, s) = \mathbb{E}[f_r(c, s)]$, and the noise on repeat r to be the residual after the expected response is subtracted: $\nu_r(c, s) = f_r(c, s) - \phi(c, s)$. By definition, the noise has zero expectation: $\mathbb{E}_{\nu_r}[\nu_r(c, s)|c, s] = 0$ for all r, c, and s. Let $\hat{\boldsymbol{u}}_n$ denote the nth PC eigenvector, computed from repeat 1.

If we estimated the variance of the projection of activity onto $\hat{\boldsymbol{u}}_n$ using a single repeat, it would contain a contribution from both the signal and the noise. However, because stimulus-independent variability is by definition uncorrelated between repeats of the same stimulus, we can obtain an unbiased estimate of the signal variance, from the covariance across these independent repeats:

$$\mathbb{E}_{\nu_1,\nu_2}\left[\frac{1}{N_s}\sum_{i=1}^{N_s}(\boldsymbol{f}_1(s_i)\cdot\hat{\boldsymbol{u}}_n)(\boldsymbol{f}_2(s_i)\cdot\hat{\boldsymbol{u}}_n)\right]$$

$$=\frac{1}{N_s}\sum_{i=1}^{N_s}(\Phi(s_i)\cdot\hat{\boldsymbol{u}}_n)^2$$

Thus, if $\boldsymbol{u}_n$ is an eigenvector of the population signal variance, the cvPCA method will produce an unbiased estimate of the signal PC variances. As shown in Supplementary Discussion 1.1, this will occur if response variability comprises a mixture of multiplicative response gain changes, correlated additive variability orthogonal to the stimulus dimensions, and uncorrelated noise. Although additive variability in the signal space could in principle downwardly bias the estimated signal variance, other studies confirm that under conditions similar to those analysed here there is little additive variability in the signal space[36]; furthermore, simulations confirm that the amount of such variability present in our recordings does not substantially bias the estimation of signal eigenspectra with cvPCA (Extended Data Fig. 5).

We ran cvPCA ten times on each dataset, on each iteration randomly sampling the population responses of each stimulus from the two repeats without replacement. Thus, $\boldsymbol{f}_1(s)$ could be the population response from either the first or the second repeat, with $\boldsymbol{f}_2(s)$ being the response from the other. The displayed eigenspectra are averages over the ten different runs.

Simulations. To verify that cvPCA method was able to accurately estimate signal eigenspectra in the presence of noise, we analysed simulated data for which the true eigenspectrum was known by construction, and stimulus responses were corrupted by noise. Mathematical analyses (Supplementary Discussion 1.1 and 3.6) showed that noise consisting of multiplicative gain modulation, additive noise orthogonal to signal dimensions, or independent additive noise should not bias the expected eigenspectrum estimate, but that correlated additive noise in the stimulus dimensions could potentially lead the eigenspectrum to be underestimated. We therefore first concentrated on this possibility.

To create the test data, we first simulated noise-free sensory responses, the eigenspectrum of which followed an exact power law, with three possible exponents: $\alpha = 0.5$, 1.0, or 1.5. To simulate the responses of $N_c = 10{,}000$ neurons to $N_s = 2{,}800$ stimuli with this exact eigenspectrum, we first constructed a set of random orthogonal eigenvectors by performing singular value decomposition on a $N_c \times N_s$ matrix A of independent standard Gaussian variates: $A = USV^T$. We created a diagonal matrix D_α, of which the nth diagonal entry was $n^{-\alpha/2}$, and created the $N_c \times N_s$ matrix of simulated noise-free responses as $\phi = UDV^T$.

Additive noise. To simulate correlated additive noise in the stimulus space (Extended Data Fig. 5c), we constructed noise for which the eigenspectrum matched that observed experimentally. To find the empirical noise eigenspectrum, we first estimated the total variance of the nth PC as

$$\hat{\Lambda}_n = \frac{1}{2}\left[\frac{1}{N_s}\sum_{i=1}^{N_s}(\boldsymbol{f}_1(s_i)\cdot\boldsymbol{u}_n)^2 + \frac{1}{N_s}\sum_{i=1}^{N_s}(\boldsymbol{f}_2(s_i)\cdot\boldsymbol{u}_n)^2\right]$$

and estimated the signal variance using cvPCA as

$$\hat{\lambda}_n = \frac{1}{N_s}\sum_{i=1}^{N_s}(\boldsymbol{f}_1(s_i)\cdot\boldsymbol{u}_n)(\boldsymbol{f}_2(s_i)\cdot\boldsymbol{u}_n)$$

The estimated noise spectrum was the difference between total variance and signal variance: $\hat{\delta}_n = \hat{\Lambda}_n - \hat{\lambda}_n$. This spectrum reflects the summed magnitude of both correlated and uncorrrelated noise in the signal dimensions, and is shown in Extended Data Fig. 5b. Responses corrupted by additive noise were simulated as $\Phi + b_\alpha U\Delta V^T$, where Δ is a diagonal matrix with entries δ_n, and the scale factor b_α ensured that, as in the data, the simulation showed a total of 14% reliable variance. The scale factors were found by search to be 2.62, 2.52, 2.41 for the signal eigenspectrum exponents $\alpha = 0.5$, 1.0, 1.5, respectively.

Multiplicative noise. To simulate multiplicative noise (Extended Data Fig. 5d), responses were multiplied by an amplitude factor that was constant across neurons, but was drawn independently for each stimulus and repeat. To simulate an appropriately skewed distribution of gains, the scale factor was distributed as 0.5 plus an exponential random variate with mean parameter c_α. The values of c_α were found by search as those matching the observed 14% reliable variance, yielding 1.55, 1.52, 1.40 for the signal eigenspectrum exponents $\alpha = 0.5$, 1.0, 1.5, respectively.

To simulate a combination of additive and multiplicative noise (Extended Data Fig. 5e), responses were modulated by the additive mechanism described above and then modulated multiplicatively. The gain factors were $b_\alpha = 0.55$, 0.53, 0.51 and $c_\alpha = 0.65$, 0.64, 0.59 for $\alpha = 0.5$, 1.0, 1.5 respectively.

Two-photon noise. To investigate whether our two-photon deconvolution method could be biasing the estimated eigenspectrum, we simulated the effect of passing noise through this algorithm (Extended Data Fig. 5f).

To do so, we extended the simulations above to apply in the time domain. When simulating the additive noise, we allowed it to vary across all simulated two-photon imaging frames (replacing the matrix A used to compute the eigenvectors U and V by a 10,000 × 8,400 matrix providing three simulated frames per stimulus presentation). The gain modulation factor was assumed equal for all three frames corresponding to a single stimulus. The magnitudes of the additive noise and the gain factor giving 14% signal variance were found by search to be $b_\alpha = 0.50$, 0.50, 0.49 and $c_\alpha = 0.68$, 0.67, 0.66, for $\alpha = 0.5$, 1.0, 1.5, respectively.

To simulate the response of GCaMP6s, we convolved these responses with an exponentially decaying kernel with a timescale of 2 s (because each time point in the data is 0.4 s, this corresponds to a decay timescale of five time points). To simulate shot noise, we added Gaussian white noise with a standard deviation of 0.5. Next we deconvolved these noisy traces using OASIS[39], with a timescale of 5 time points and no sparsity constraints. The reduction in signal variance from this procedure was roughly 1%.

For all noise simulations, we estimated the signal eigenspectrum from two repeats using cvPCA. We found that cvPCA, but not ordinary PCA, correctly estimated the ground-true eigenspectrum, for all simulated power-law exponents α (Extended Data Fig. 5g).

Estimation of power-law exponent. We computed the linear fit of the eigenspectrum over the range of 11 to 500 dimensions for all recordings (and model fits) other than the 32 drifting grating recordings. For the 32-grating recordings, owing to noise and the length of the spectrum, we computed the power-law exponent from 5 to 30. The linear fit was performed in log–log space: the range of log(11) to log(500) was regressed onto the log of the eigenspectrum, sampled at points that were themselves logarithmically spaced between 11 and 500.

Sorting neurons and stimuli by correlations. In Extended Data Fig. 6, neurons and stimuli were sorted so that they were close to other neurons and stimuli with which they were correlated.

To do this, we first z-scored the binned activity of each neuron and computed PCs of its averaged activity across repeats. Each panel shows this for different PC projections of the data: 1, 2, 3–10, 11–40, 41–200 and 201–1,000. Stimuli were re-ordered so that the pattern of evoked population activity of each stimulus was most similar to the average of its neighbours. The stimulus order was initialized by sorting stimuli according to their weights on the top PC of activity, then dividing them into 30 clusters of equal size along this ordering. For 50 iterations, we computed the mean activity of each cluster and smoothed this activity across clusters with a Gaussian, the width of which was annealed from 6 clusters to 1 over the first 25 iterations. Each stimulus was then reassigned to the cluster it was most correlated with. On the final pass, we upsampled the correlations of the stimuli with each cluster by a factor of 100 using kriging interpolation (smoothing constant of 1 cluster), resulting in a continuous assignment of stimuli along the 1D axis of the clustering algorithm. After sorting across stimuli, we smoothed across them to reduce noise, recomputed the PCs on the activity smoothed across stimuli, and repeated the procedure to sort neurons. The algorithm is available in Python and MATLAB at https://www.github.com/MouseLand/RasterMap. These plots were made using the MATLAB version of the code.

Reporting summary. Further information on research design is available in the Nature Research Reporting Summary linked to this paper.

Data availability

All of the processed deconvolved calcium traces are available on figshare[41] (https://figshare.com/articles/Recordings_of_ten_thousand_neurons_in_visual_cortex_in_response_to_2_800_natural_images/6845348), together with the image stimuli.

Code availability

The code is available on GitHub (https://github.com/MouseLand/stringer-pachitariu-et-al-2018b).

36. Stringer, C. et al. Spontaneous behaviors drive multidimensional, brainwide activity. *Science* **364**, eaav7893 (2019).
37. Pologruto, T. A., Sabatini, B. L. & Svoboda, K. ScanImage: flexible software for operating laser scanning microscopes. *Biomed. Eng. Online* **2**, 13 (2003).
38. Chen, T.-W. et al. Ultrasensitive fluorescent proteins for imaging neuronal activity. *Nature* **499**, 295–300 (2013).
39. Friedrich, J., Zhou, P. & Paninski, L. Fast online deconvolution of calcium imaging data. *PLoS Comput. Biol*. **13**, e1005423 (2017).
40. Pachitariu, M., Stringer, C. & Harris, K. D. Robustness of spike deconvolution for neuronal calcium imaging. *J. Neurosci*. **38**, 7976–7985 (2018).
41. Stringer, C., Pachitariu, M., Carandini, M. & Harris, K. Responses of ten thousand neurons to 2,800 natural images. *Figshare* https://doi.org/10.25378/janelia.6845348.v3 (2018).
42. Jun, J. J. et al. Fully integrated silicon probes for high-density recording of neural activity. *Nature* **551**, 232–236 (2017).
43. Pachitariu, M., Steinmetz, N. A., Kadir, S. N., Carandini, M. & Harris, K. D. Fast and accurate spike sorting of high-channel count probes with kilosort. In *Advances in Neural Information Processing Systems* 4448–4456 (2016).
44. Allen, W. E. et al. Thirst regulates motivated behavior through modulation of brainwide neural population dynamics. *Science* **364**, eaav3932(2019).
45. Izenman, A. J. Reduced-rank regression for the multivariate linear model. *J. Multivariate Anal*. **5**, 248–264 (1975).
46. Schwartz, O. & Simoncelli, E. P. Natural signal statistics and sensory gain control. *Nat. Neurosci*. **4**, 819–825 (2001).
47. Cowley, B. R., Smith, M. A., Kohn, A. & Yu, B. M. Stimulus-driven population activity patterns in macaque primary visual cortex. *PLoS Comput. Biol*. **12**, e1005185 (2016).
48. Gallego, J. A. et al. Cortical population activity within a preserved neural manifold underlies multiple motor behaviors. *Nat. Commun*. **9**, 4233 (2018).

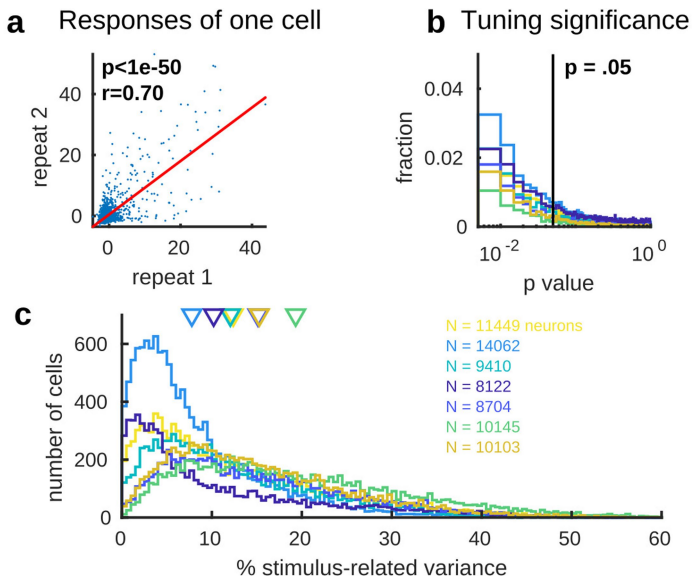

Extended Data Fig. 1 | Reliability of single-neuron responses. **a**, The responses of a single neuron to the first repeat of 2,800 stimuli plotted against its responses to the second repeat of the same stimuli. **b**, Histograms of *P* values for Pearson correlation of responses on the two repeats. Each coloured histogram represents a different recording. In total, 81.4 ± 5.1% (mean ± s.e.m., $n = 7$ recordings) of cells were significant at $P < 0.05$. **c**, Histogram of the single-neuron percentage of stimulus-related variance across the population. Each coloured histogram represents a different recording; arrowheads (top) represent the mean for each experiment.

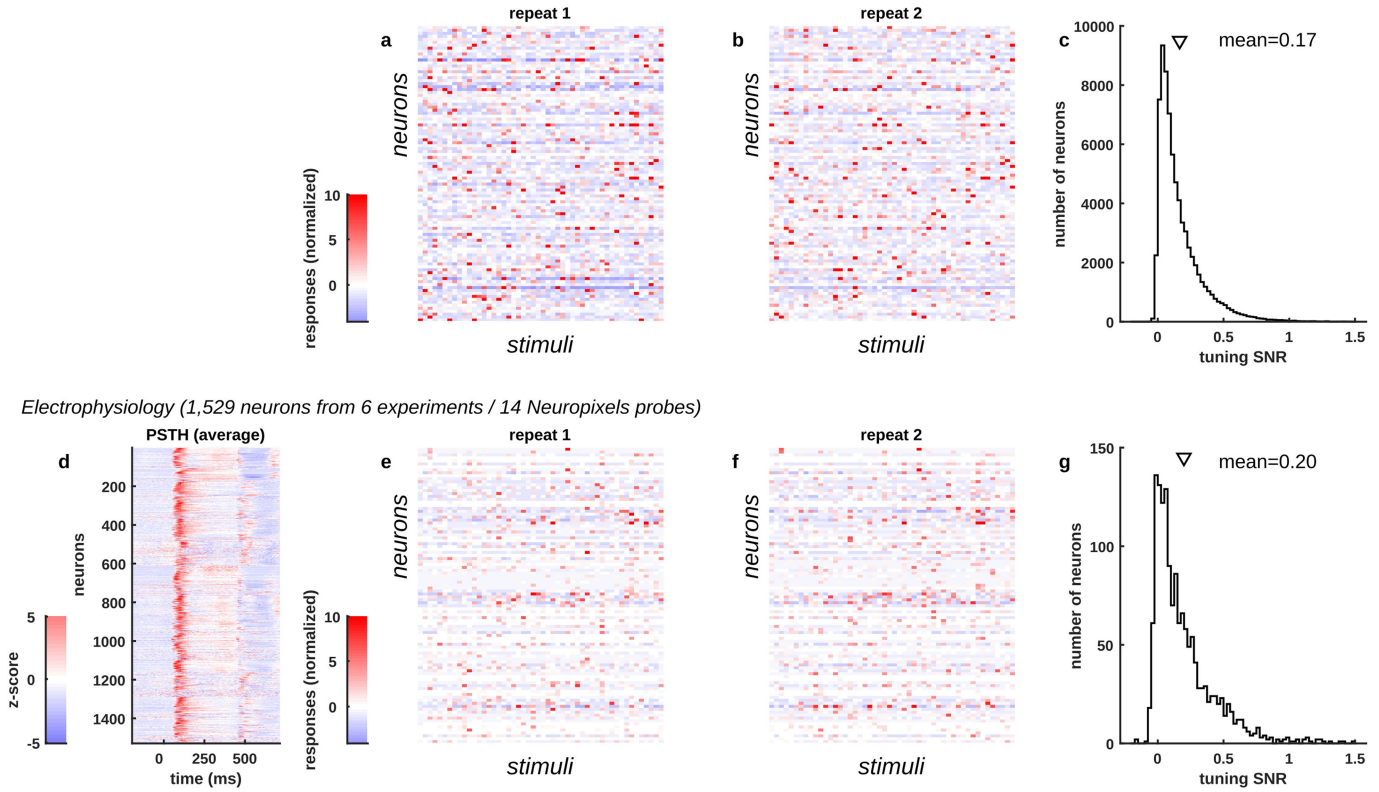

Extended Data Fig. 2 | Comparison with electrophysiology. a, **b**, Single trial responses of 100 neurons to two repeats of 50 stimuli, recorded by two-photon calcium imaging. **c**, Distribution of tuning SNR for 74,353 neurons recorded by two-photon calcium imaging. **d**, Average peristimulus time histogram of spikes recorded electrophysiologically in a separate set of experiments. The images shown were a random subset of 700 images out of the total 2,800. The peristimulus time histogram reflects the average over all stimuli. The responses are *z*-scored across time for each neuron. **e**–**g**, Same as **a**–**c** for the electrophysiologically recorded neurons.

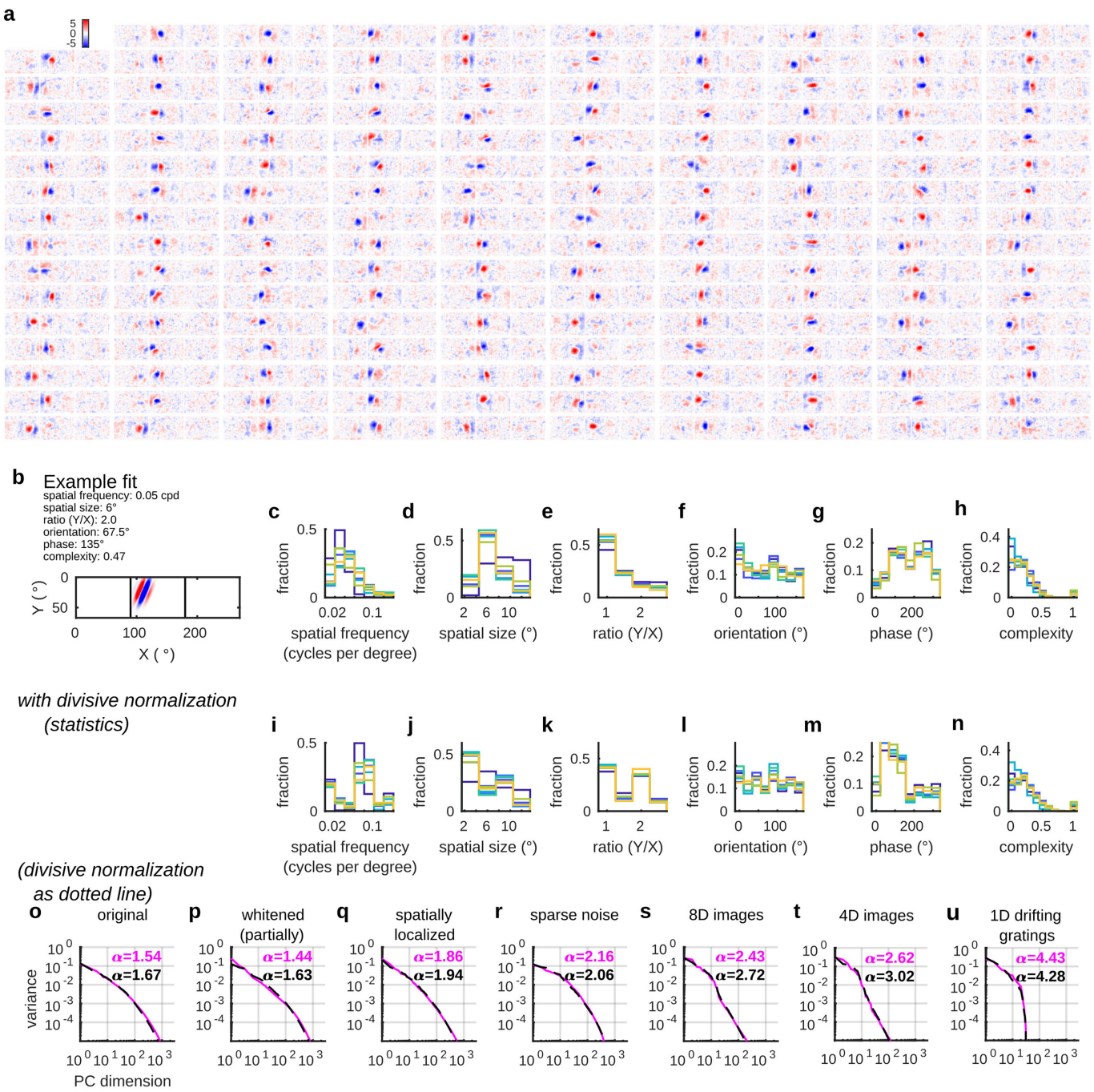

Extended Data Fig. 3 | Single-neuron receptive fields estimated using reduced-rank regression and Gabor models. a, The receptive fields of 159 randomly chosen neurons, estimated using reduced-rank regression. The receptive field map is *z*-scored for each neuron. **b**, An example Gabor fit to a single cell. **c**–**h**, Histograms showing the distribution of model parameters across cells. Each colour represents cells from one recording. **i**–**n**, Histograms showing the distribution of model parameters across cells when the model also has divisive normalization. **o**–**u**, Eigenspectra of Gabor population model responses to the different stimulus sets, as labelled. The unnormalized Gabors are shown in magenta, and the model with divisive normalization in black.

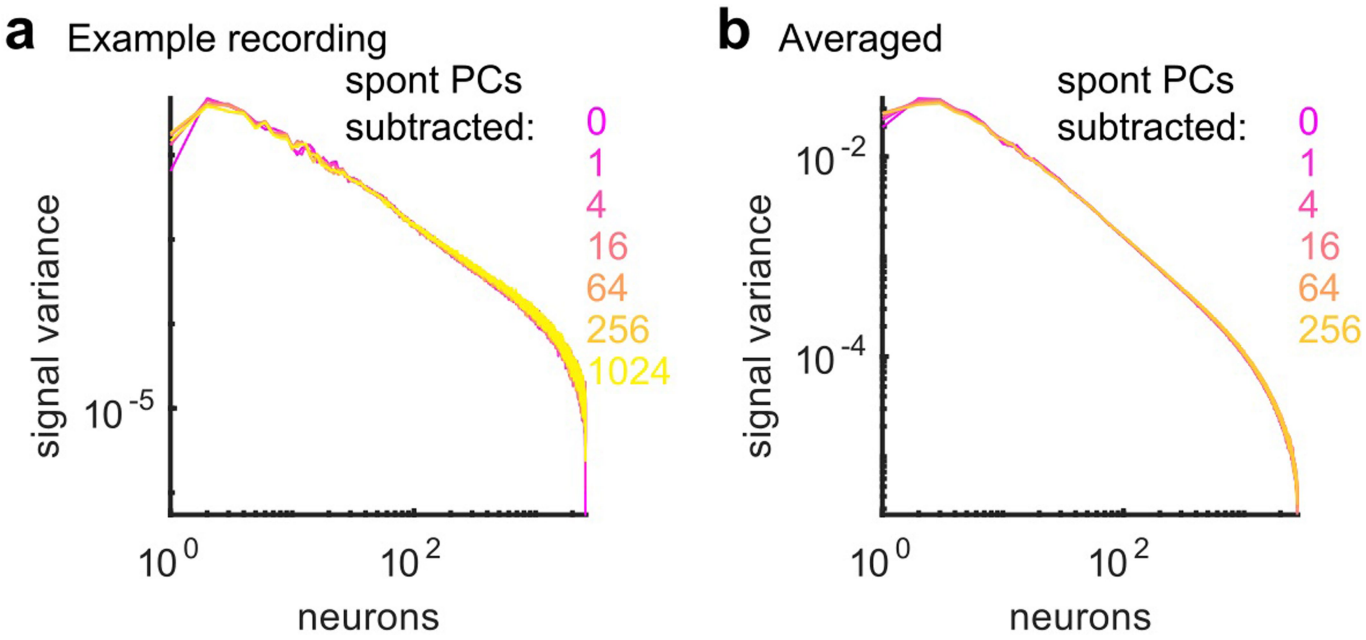

Extended Data Fig. 4 | Stimulus-independent activity does not affect the measured eigenspectrum. a, To measure the effects of correlated noise variability on eigenspectra estimated by cvPCA, we examined the effect of projecting out different numbers of noise dimensions (estimated during periods of spontaneous grey-screen) from the responses in an example experiment. **b**, The same analysis as in **a**, averaged over all recordings. The presence of these noise dimensions made little difference to the estimated signal eigenspectrum other than to slightly reduce estimated eigenvalues in the highest and lowest dimensions. For the main analyses, 32 spontaneous dimensions were subtracted.

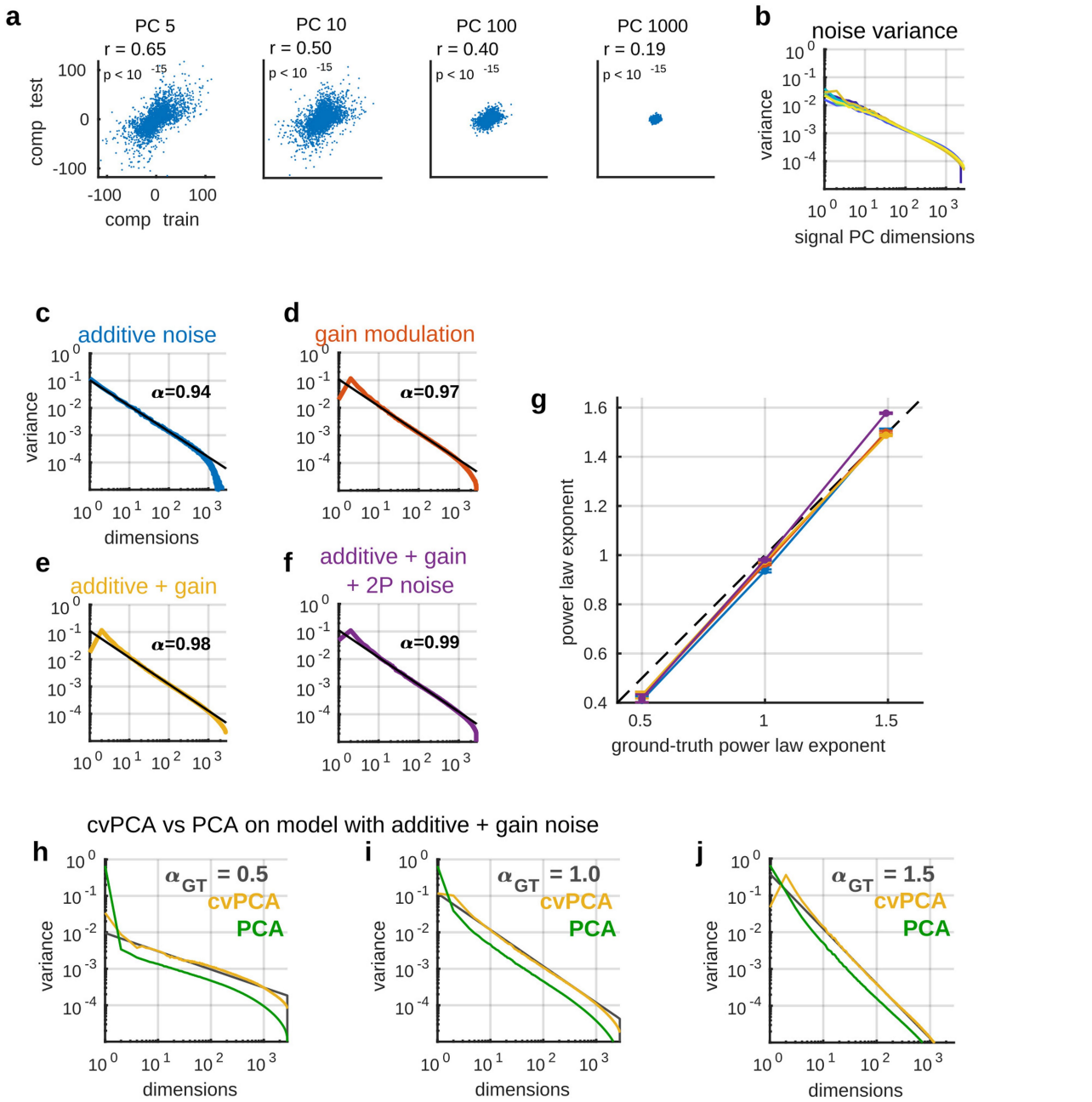

Extended Data Fig. 5 | Validating the eigenspectrum estimation method using simulations with the true noise distribution. a, Scatterplots illustrating the noise levels of each estimated PC. Each plot shows population activity projected onto the specified PC, for the first repeat (x axis) and second repeat (y axis). Each point represents responses to a single stimulus. **b**, Estimated level of noise variance in successive signal dimensions. Noise variance was estimated by subtracting the cvPCA estimate of signal variance from the total variance (see Methods). **c**, Recovery of ground-truth eigenspectrum in simulated data. We simulated responses of 10,000 neurons to 2,800 stimuli with a power spectrum decay of exactly $\alpha = 1$, and added noise in the stimulus space, generated with the spectrum in **b** scaled to produce the same signal-to-noise ratio as in the original neural data. The ground-truth eigenspectrum (black) is estimated accurately by the cvPCA method (blue). **d**, Same analysis as in **c** with multiplicative noise, in which the responses of all neurons on each trial were multiplied by a common random factor. The distribution of this factor was again scaled to recover the original signal-to-noise ratio. **e**, Same analysis as in **c** with a combination of multiplicative and additive noise. **f**, Same analysis as in **c**, also including simulation of neural and two-photon shot noise before running a GCaMP deconvolution algorithm. **g**, Ten instantiations of the simulation were performed with ground-truth exponents of 0.5, 1.0 and 1.5. Error bars represent standard deviations of the power-law exponents estimated for each of the ten simulations. The dashed black line represents the ground-truth value. **h**–**j**, Comparison of cvPCA (yellow) and traditional PCA (green) algorithms in the presence of the additive + multiplicative noise combination. Whereas cvPCA recovered the ground-truth eigenspectrum (black) exactly, traditional PCA did not, resulting in overestimation of the top eigenvalues and failure to detect the ground-truth power law.

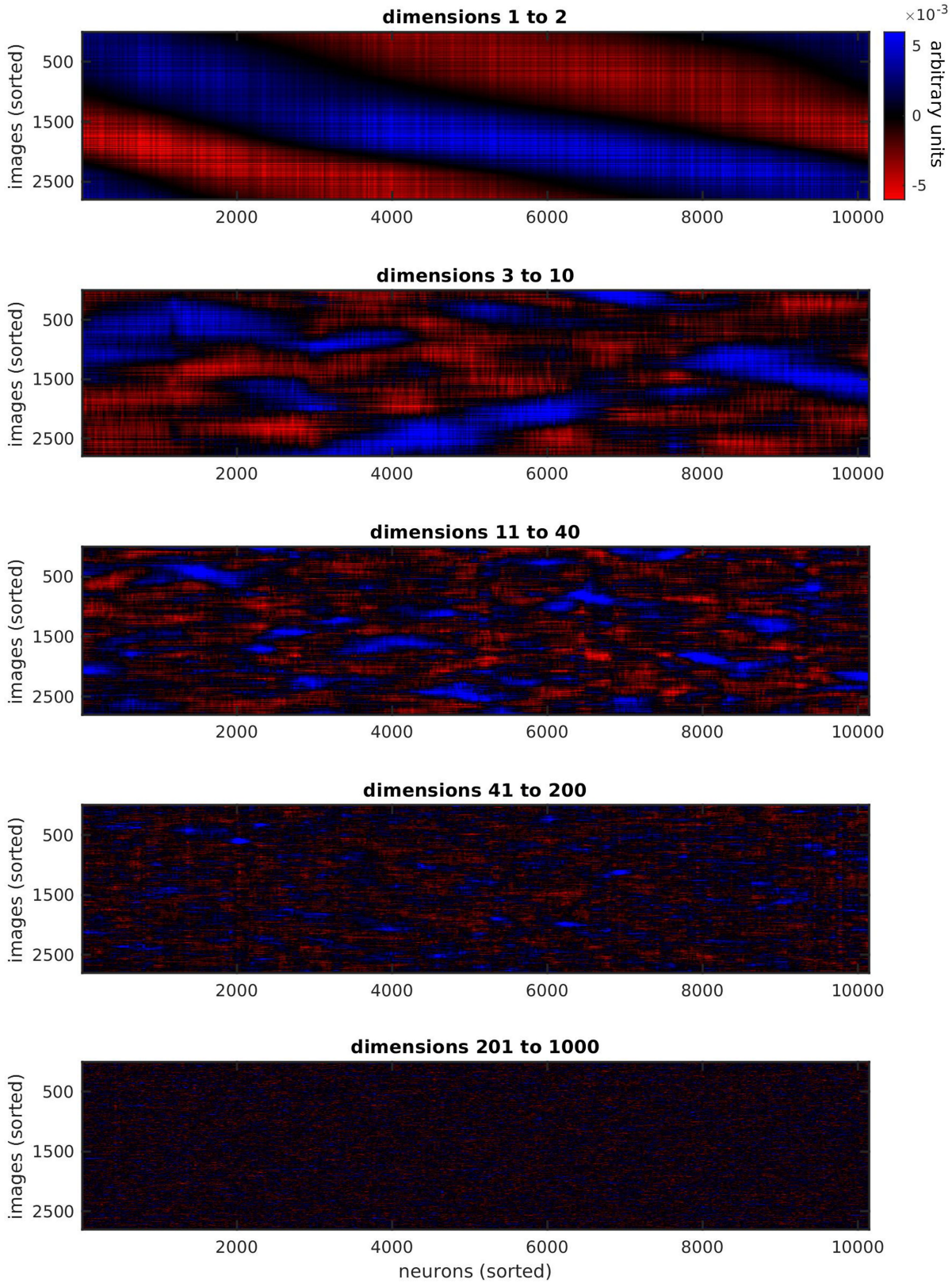

Extended Data Fig. 6 | Successive PC dimensions encode finer stimulus features. Each plot shows the responses of 10,145 neurons to 2,800 natural images, projected onto the specified PCs and then sorted along both axes so that correlated neurons and stimuli are close together. We then smoothed the matrix across neurons and stimuli with Gaussian kernels of widths of 8 neurons and 2 stimuli, respectively. Dimensions 1–2 reveal a coarse, one-dimensional organization of the neurons and stimuli. Dimensions 3–10 reveal multidimensional structure, which involves different neural subpopulations responding to different stimuli. Dimensions 11–40 reveal finer-structured patterns of correlated selectivity among neurons. Dimensions 41–200 and 201–1,000 reveal even finer-structured selectivity, which contained less neural variance.

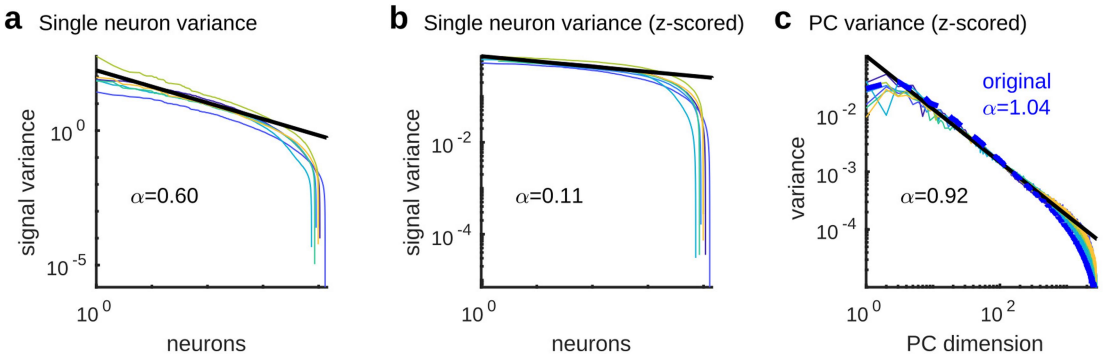

Extended Data Fig. 7 | Power-law scaling reflects correlation structure, not single-neuron statistics. a, The signal variance of the responses of each neuron are sorted in descending order; they approximately follow a power law with a decay exponent of $\alpha = 0.59$. **b**, The same plot after *z*-scoring the recorded traces to equalize stimulus response sizes between cells; the distribution of single-neuron variance has become nearly flat. **c**, PC eigenspectra for *z*-scored data. Each coloured line represents a different recording. The dashed blue line shows the average eigenspectrum from the original, non-*z*-scored responses. The fact that the eigenspectrum power law is barely affected by equalizing firing rates, whereas the distribution of single-cell signal variance is altered, indicates that the power law arises from correlations between cells rather than from the distribution of firing rates or signal variance across cells.

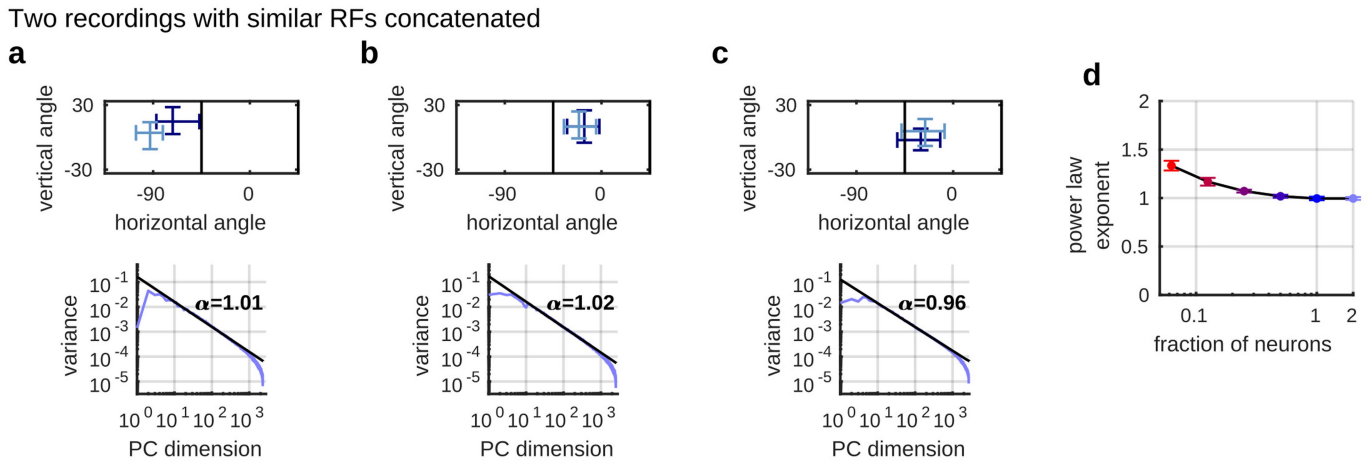

Extended Data Fig. 8 | Power-law eigenspectra in concatenated recordings. a–c, To investigate whether power-law eigenspectra apply to even larger populations, we were able to artificially double the number of recorded neurons by combining three pairs of recordings for which the imaging fields of view had similar retinotopic locations. Top, retinotopic locations of receptive fields (95% confidence intervals on the mean receptive field position of that recording), with each recording shown in a different shade of blue. Bottom, eigenspectrum of concatenated recordings in response to the 2,800 natural image stimuli; total population sizes 19,571, 23,472 and 18,807 cells respectively. Each panel (**a**, **b** and **c**) represents one pair of recordings. **d**, Eigenspectrum exponents for random subsets of the combined populations (compare with Fig. 2j). The horizontal axis shows the population size relative to single recordings, so the merged population has size 2. The mean power-law exponent for fraction of neurons = 2 was $\alpha = 0.99 \pm 0.02$ (mean ± s.e.m.).

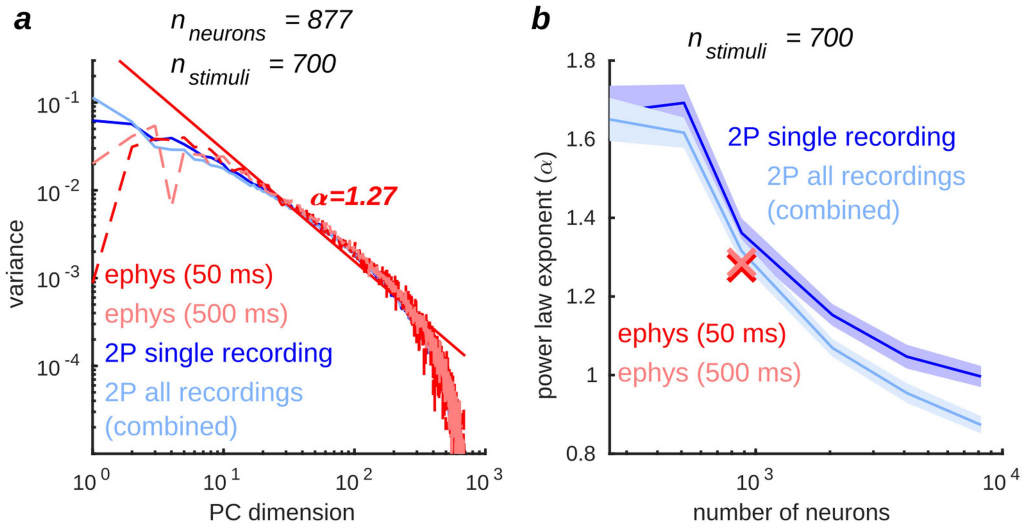

Extended Data Fig. 9 | Eigenspectrum of electrophysiologically recorded data. We recorded neural activity electrophysiologically in response to 700 out of the 2,800 stimuli, and concatenated the recordings, resulting in a total of 877 neurons recorded across 6 experiments. **a**, With this smaller number of stimuli and neurons, convergence to a power law is not complete, and the exponent cannot be estimated accurately (compare with Fig. 2g–j). We therefore compared the electrophysiology data to the responses generated by these stimuli in 877 neurons sampled randomly from either a single two-photon imaging experiment (dark blue) or all experiments combined (light blue). The red and pink colours show electrophysiology eigenspectra with time bins of 50 ms or 500 ms; the red line shows the best linear fit to estimate the exponent. **b**, The blue curves represent power-law exponents estimated from the responses of different-sized neuronal subpopulations to this set of 700 stimuli; the shading represents s.e.m. over different random subsets of neurons. The red and pink crosses denote estimated exponents from electrophysiology data for 50-ms and 500-ms bin sizes.

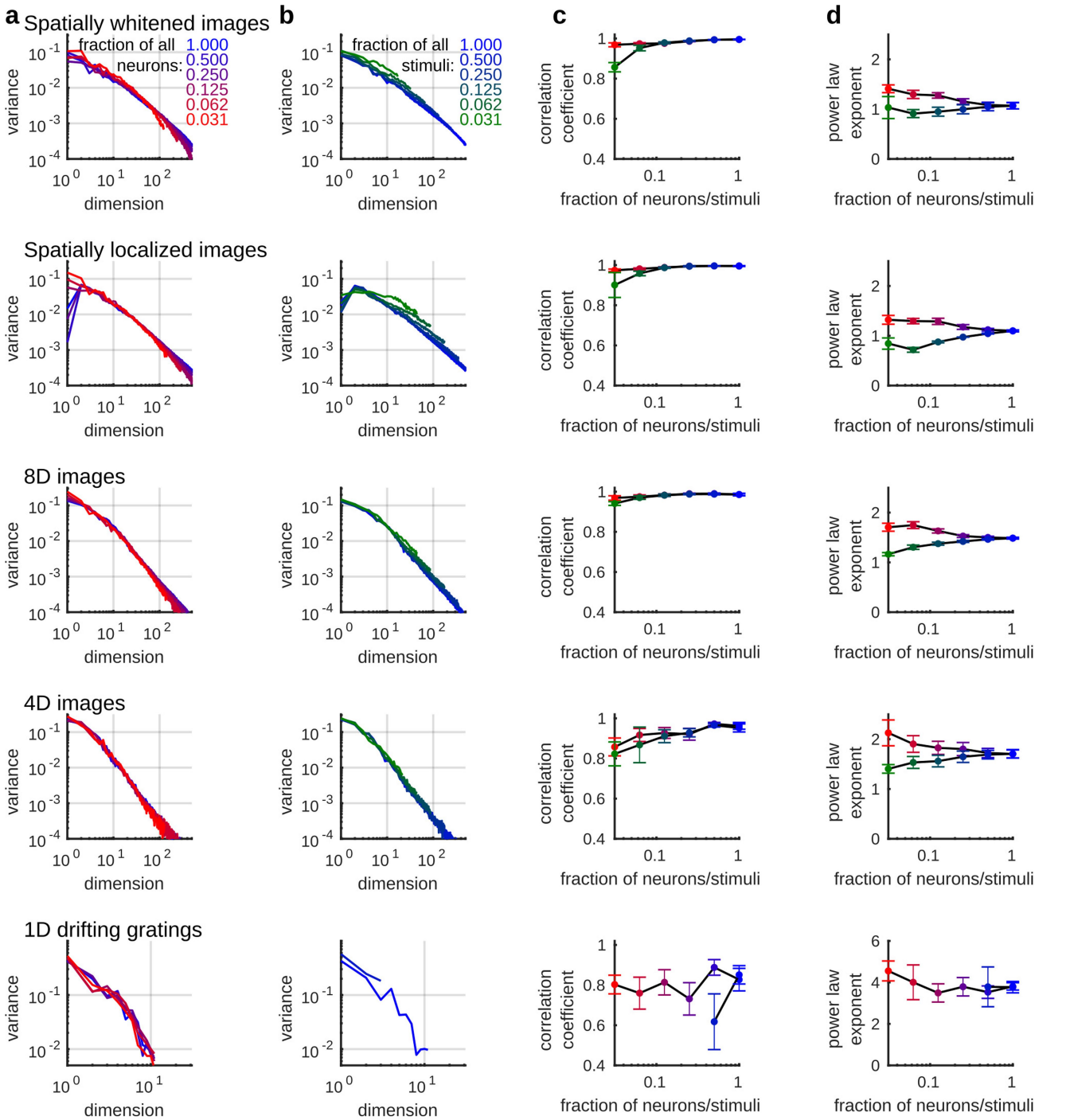

Extended Data Fig. 10 | Power-law scaling grows more accurate for increasing numbers of neurons and stimuli, for all stimulus ensembles. **a**, Eigenspectra estimated from a random subset of the recorded neurons, colour-coded by the fraction of neurons retained. **b**, Eigenspectra estimated from a random subset of stimuli, colour-coded by the fraction of stimuli retained. **c**, Correlation coefficient of the spectra plotted in **a**, **b**. **d**, Power-law exponent of the spectra plotted in **a**, **b**. Each row corresponds to a different ensemble of visual stimuli.

nature research

Corresponding author(s): Carsen Stringer, Marius Pachitariu, Kenneth Harris

Last updated by author(s): Apr 22, 2019

Reporting Summary

Nature Research wishes to improve the reproducibility of the work that we publish. This form provides structure for consistency and transparency in reporting. For further information on Nature Research policies, see Authors & Referees and the Editorial Policy Checklist.

Statistics

For all statistical analyses, confirm that the following items are present in the figure legend, table legend, main text, or Methods section.

n/a	Confirmed	
☐	☒	The exact sample size (*n*) for each experimental group/condition, given as a discrete number and unit of measurement
☐	☒	A statement on whether measurements were taken from distinct samples or whether the same sample was measured repeatedly
☐	☒	The statistical test(s) used AND whether they are one- or two-sided *Only common tests should be described solely by name; describe more complex techniques in the Methods section.*
☒	☐	A description of all covariates tested
☒	☐	A description of any assumptions or corrections, such as tests of normality and adjustment for multiple comparisons
☐	☒	A full description of the statistical parameters including central tendency (e.g. means) or other basic estimates (e.g. regression coefficient) AND variation (e.g. standard deviation) or associated estimates of uncertainty (e.g. confidence intervals)
☐	☒	For null hypothesis testing, the test statistic (e.g. *F*, *t*, *r*) with confidence intervals, effect sizes, degrees of freedom and *P* value noted *Give P values as exact values whenever suitable.*
☒	☐	For Bayesian analysis, information on the choice of priors and Markov chain Monte Carlo settings
☒	☐	For hierarchical and complex designs, identification of the appropriate level for tests and full reporting of outcomes
☐	☒	Estimates of effect sizes (e.g. Cohen's *d*, Pearson's *r*), indicating how they were calculated

Our web collection on statistics for biologists contains articles on many of the points above.

Software and code

Policy information about availability of computer code

Data collection	We used the open-source Scanimage v4.2 software for two-photon calcium imaging data acquisition (http://scanimage.vidriotechnologies.com/display/SIH/ScanImage+Home). Electrophysiological acquisition was done using the open-source SpikeGLX software (https://billkarsh.github.io/SpikeGLX/).
Data analysis	We processed the two-photon calcium imaging data using suite2p (github.com/MouseLand/suite2p) and the electrophysiological data using Kilosort2 (github.com/MouseLand/kilosort2). The one-dimensional visualization used rastermap (github.com/MouseLand/rastermap). All the code to reproduce the figures is provided at github.com/MouseLand/stringer-pachitariu-et-al-2018b.

For manuscripts utilizing custom algorithms or software that are central to the research but not yet described in published literature, software must be made available to editors/reviewers. We strongly encourage code deposition in a community repository (e.g. GitHub). See the Nature Research guidelines for submitting code & software for further information.

Data

Policy information about availability of data

All manuscripts must include a data availability statement. This statement should provide the following information, where applicable:

- Accession codes, unique identifiers, or web links for publicly available datasets
- A list of figures that have associated raw data
- A description of any restrictions on data availability

All the processed two-photon calcium imaging is provided on figshare: https://figshare.com/articles/Recordings_of_ten_thousand_neurons_in_visual_cortex_in_response_to_2_800_natural_images/6845348.

Field-specific reporting

Please select the one below that is the best fit for your research. If you are not sure, read the appropriate sections before making your selection.

☒ Life sciences ☐ Behavioural & social sciences ☐ Ecological, evolutionary & environmental sciences

For a reference copy of the document with all sections, see nature.com/documents/nr-reporting-summary-flat.pdf

Life sciences study design

All studies must disclose on these points even when the disclosure is negative.

Sample size	The sample size was sufficiently large (8 mice from which 42 recordings containing ~10,000 neurons each were performed).
Data exclusions	We excluded two recordings which did not have significant signal variance, suggesting we were not recording in primary visual cortex.
Replication	We observed similar results across mice in terms of the power law decay of signal variance across dimensions.
Randomization	This is not relevant to our study because it is an observational study looking at the activity of neurons in visual cortex in healthy awake adult mice.
Blinding	Blinding was not relevant to our study (see above).

Reporting for specific materials, systems and methods

We require information from authors about some types of materials, experimental systems and methods used in many studies. Here, indicate whether each material, system or method listed is relevant to your study. If you are not sure if a list item applies to your research, read the appropriate section before selecting a response.

Materials & experimental systems

n/a	Involved in the study
☒	☐ Antibodies
☒	☐ Eukaryotic cell lines
☒	☐ Palaeontology
☐	☒ Animals and other organisms
☒	☐ Human research participants
☒	☐ Clinical data

Methods

n/a	Involved in the study
☒	☐ ChIP-seq
☒	☐ Flow cytometry
☒	☐ MRI-based neuroimaging

Animals and other organisms

Policy information about studies involving animals; ARRIVE guidelines recommended for reporting animal research

Laboratory animals	We used mice bred to express GCaMP6s in excitatory neurons in our recordings: 13 recordings from TetO-GCaMP6s x Emx1-IRES-Cre mice (available as JAX 024742 and JAX 005628); 3 recordings from a Camk2a-tTA, Ai94 GCaMP6s 2tg x Emx1-IRES-Cre mouse (available as JAX 024115 and JAX 005628); and 2 recordings from a Camk2a-tTA, Ai94 GCaMP6s 2tg x Rasgrf-Cre mouse (available as JAX 024115 and JAX 022864). We also used mice bred to express tdTomato in inhibitory neurons (GAD-IRES-Cre x CAG-tdTomato, available as JAX 010802 and JAX 007909) in 14 recordings. These mice were male and female, and ranged from age 2 to 8 months.
Wild animals	*Provide details on animals observed in or captured in the field; report species, sex and age where possible. Describe how animals were caught and transported and what happened to captive animals after the study (if killed, explain why and describe method; if released, say where and when) OR state that the study did not involve wild animals.*
Field-collected samples	*For laboratory work with field-collected samples, describe all relevant parameters such as housing, maintenance, temperature, photoperiod and end-of-experiment protocol OR state that the study did not involve samples collected from the field.*
Ethics oversight	All experimental procedures were conducted according to the UK Animals Scientific Procedures Act (1986). Experiments were performed at University College London under personal and project licenses released by the Home Office following appropriate ethics review.

Note that full information on the approval of the study protocol must also be provided in the manuscript.